

Monte Carlo simulations and experiments of Bessel beams and tissue-like phantoms  
interaction

by

Jianing Yang

A thesis submitted in partial fulfillment  
of the requirements for the degree of  
Master of Applied Science (M.A.Sc) in Natural Resources Engineering

The Faculty of Graduate Studies  
Laurentian University  
Sudbury, Ontario, Canada

© Jianing Yang, 2016

**THESIS DEFENCE COMMITTEE/COMITÉ DE SOUTENANCE DE THÈSE**  
**Laurentian Université/Université Laurentienne**  
Faculty of Graduate Studies/Faculté des études supérieures

Title of Thesis Titre de la thèse	Monte Carlo simulations and experiments of Bessel beams and tissue-like phantoms		
Name of Candidate Nom du candidat	Yang, Jianing		
Degree Diplôme	Master of Applied Science		
Department/Program Département/Programme	Natural Resources Engineering	Date of Defence Date de la soutenance	February 23, 2017

**APPROVED/APPROUVÉ**

Thesis Examiners/Examineurs de thèse:

Dr. Brahim Chebbi  
(Supervisor/Directeur(trice) de thèse)

Dr. Helen Shang  
(Committee member/Membre du comité)

Dr. Junfeng Zhang  
(Committee member/Membre du comité)

Dr Ilya Golub  
(External Examiner/Examineur externe)

Approved for the Faculty of Graduate Studies  
Approuvé pour la Faculté des études supérieures  
Dr. David Lesbarrères  
Monsieur David Lesbarrères  
Dean, Faculty of Graduate Studies  
Doyen, Faculté des études supérieures

**ACCESSIBILITY CLAUSE AND PERMISSION TO USE**

I, **Jianing Yang**, hereby grant to Laurentian University and/or its agents the non-exclusive license to archive and make accessible my thesis, dissertation, or project report in whole or in part in all forms of media, now or for the duration of my copyright ownership. I retain all other ownership rights to the copyright of the thesis, dissertation or project report. I also reserve the right to use in future works (such as articles or books) all or part of this thesis, dissertation, or project report. I further agree that permission for copying of this thesis in any manner, in whole or in part, for scholarly purposes may be granted by the professor or professors who supervised my thesis work or, in their absence, by the Head of the Department in which my thesis work was done. It is understood that any copying or publication or use of this thesis or parts thereof for financial gain shall not be allowed without my written permission. It is also understood that this copy is being made available in this form by the authority of the copyright owner solely for the purpose of private study and research and may not be copied or reproduced except as permitted by the copyright laws without written authority from the copyright owner.

## **Abstract**

In this thesis, the propagation of Bessel beam in tissue and its potential advantages were explored numerically and experimentally. In the numerical simulations, the Monte Carlo method is used to simulate the propagation of Gaussian and Bessel beams in tissue. By convolving the impulse profile generated by a pencil beam's propagation with either beam intensity profile, the response of the propagation of the said beam can be approximated. This process was done by modifying and using MCML and CONV software which are available from the literature. Experimentally, the Bessel beams were generated by a laser and axicons, and made to propagate through optical phantoms formed with variable density intralipid solutions. The intensity distribution of the transmitted Bessel beam at the exit of the scattering media was measured and compared with transmittance results from simulation. At last, a separate experiment was designed to investigate the reconstruction of a Bessel beam after it passes the optical phantom.

## **Keywords**

Laser, Bessel beam, Monte Carlo method, convolution, light tissue interaction, tissue-like phantom, optical properties, self-healing.

## Table of content

Abstract .....	iii
Keywords .....	iii
Table of content .....	iv
Table of tables .....	viii
Table of figures .....	x
Nomenclature .....	xiii
Chapter 1 Introduction .....	1
1.1 Background .....	1
1.2 Objective .....	2
1.3 Scope .....	3
Chapter 2 Literature review .....	5
2.1 Tissue-like phantoms.....	5
2.2 Techniques to determine the optical properties of tissue-like samples .....	6
2.3 Bessel beams and axicons .....	8
2.4 Simulation of light propagation in tissue .....	8
2.5 Experimental investigations of laser beams propagating in tissue-like medium ....	10
Chapter 3 Optical and light scattering properties of tissue .....	12
3.1 Optical properties .....	12
3.1.1 Optical properties' definitions .....	12

3.1.2 Optical properties determination methods.....	14
3.2 Optical properties determination for 10% intralipid .....	14
3.2.1 Index of refraction .....	15
3.2.2 Absorption coefficient .....	16
3.2.3 Scattering anisotropy .....	16
3.2.4 Scattering coefficient.....	17
3.3 Optical properties of intralipid samples .....	17
3.3.1 Mie theory.....	18
3.3.2 Application of Mie theory .....	20
3.3.3 Absorption coefficients.....	21
3.3.4 Index of refraction .....	21
Chapter 4 Simulation techniques .....	23
4.1 Software .....	23
4.3 Methods.....	27
4.3.1 Bessel beam profile .....	28
4.3.2 Initial intensity .....	28
4.3.3 Convolution .....	30
Chapter 5 Simulation results.....	31
5.1 Single layer simulations .....	31
5.1.1 Simulation with Aorta sample .....	34

5.1.2 Simulation with blood sample .....	38
5.1.3 Simulation with epidermis sample .....	39
5.1.4 Simulation with dermis sample .....	40
5.2 Multilayered simulations.....	41
5.2.1 Artery system simulation.....	42
5.2.2 Integumentary system simulation.....	43
5.3 Intralipid simulations.....	44
Chapter 6 Experimental investigation.....	52
6.1 Experimental setup.....	52
6.1.1 Supplies .....	53
6.1.2 Bessel beam specification.....	53
6.2. Procedures and Methods .....	54
6.2.1 Varying concentrations.....	54
6.2.2 Self-healing property investigation .....	58
6.4. Discussion .....	64
6.5. Conclusion.....	64
Chapter 7 Analysis.....	66
7.1 Various concentrations.....	66
7.1.1 Bessel beam characterization.....	66
7.1.2 Comparison of simulation and experimental results .....	70

7.2 Self-healing properties .....	74
7.2.1 Self-reconstructive region.....	74
7.2.2 Experimental results analysis .....	75
Chapter 8 Conclusions .....	80
Appendix A.....	82
A.1 Optical properties determination for 10% intralipid solutions.....	82
A.1.1 Index of refraction .....	82
A.1.2 Absorption coefficient .....	83
A.1.3 Scattering anisotropy .....	84
A.1.4 Scattering coefficient.....	85
Reference .....	86

## Table of tables

Table 3.1 Coefficients for calculation of the absorption coefficient .....	16
Table 3.2 Coefficients for calculation of the Scattering anisotropy .....	17
Table 3.3 Coefficients for calculation of the Scattering coefficient .....	17
Table 3.4 Optical properties of 10% intralipid under wavelength of 473nm .....	17
Table 3.5 Parameters of the experimental samples.....	20
Table 3.6 Optical properties of intralipid samples.....	22
Table 4.1 Physical quantities to be computed in MCML .....	25
Table 5.1 Tissue samples' optical properties (adapted from [35]) .....	32
Table 5.2 MCML input file template with aorta parameters .....	32
Table 5.3 Beam profile for CONV .....	34
Table 5.4 MCML input file for blood sample.....	39
Table 5.5 MCML input file for epidermis sample .....	40
Table 5.6 MCML input file for dermis sample.....	41
Table 5.7 MCML input file for artery sample .....	42
Table 5.8 MCML input file for skin sample .....	43
Table 5.9 Inputs profile for CONV.....	45
Table 5.10 MCML input file for intralipid 0.1% sample.....	46
Table 5.11 MCML input file for intralipid 0.125% sample.....	47
Table 5.12 MCML input file for intralipid 0.15% sample.....	48
Table 5.13 MCML input file for intralipid 0.175% sample.....	49
Table 5.14 MCML input file for intralipid 0.2% sample.....	50
Table 6.1 Supplies list.....	53

Table 6.2 Laser specification .....	53
Table 7.1 Theoretical fringe spacing for Bessel beams intensity .....	69
Table 7.2 Spot radius and fringe spacing calculation from experimental profiles of Bessel beam exiting 0.1% intralipid solution.....	70
Table 7.3 Spacing results comparison .....	70
Table 7.4 Minimum distance for the beam to reconstruct .....	78

## Table of figures

Figure 4.1 Schematic of beam tissue interaction modeled in MCML .....	24
Figure 4.2 MCML algorithm (Adapted from [20]).....	26
Figure 4.3 MCML output.....	27
Figure 5.1 Diffuse reflectance for a Gaussian beam ( $r=0.0042\text{cm}$ ) (Aorta).....	35
Figure 5.2 Transmittance for a Gaussian beam ( $r=0.0042\text{cm}$ ) (Aorta).....	35
Figure 5.3 Fluence at surface and half depth of the sample layer for a Gaussian beam ( $r=0.0042\text{cm}$ ) (Aorta).....	36
Figure 5.4 Contour plot of the fluence for a Gaussian beam ( $r=0.0042\text{cm}$ ) (Aorta) .....	36
Figure 5.5 Aorta simulation results comparison: reflectance, transmittance and fluence	38
Figure 5.6 Blood simulation results comparison reflectance and fluence .....	39
Figure 5.7 Epidermis simulation results comparison reflectance and fluence.....	40
Figure 5.8 Dermis simulation results comparison reflectance and fluence .....	41
Figure 5.9 Artery system and Integumentary system models.....	42
Figure 5.10 Artery simulation results comparison reflectance and fluence.....	43
Figure 5.11 Skin simulation results comparison: reflectance and fluence.....	44
Figure 5.12 0.1% intralipid simulation results comparison: reflectance, transmittance and fluence.....	46
Figure 5.13 0.125% intralipid simulation results comparison: reflectance, transmittance and fluence .....	47
Figure 5.14 0.15% intralipid simulation results comparison: reflectance, transmittance and fluence .....	48

Figure 5.15 0.175% intralipid simulation results comparison: reflectance, transmittance and fluence .....	49
Figure 5.16 0.2% intralipid simulation results comparison: reflectance, transmittance and fluence.....	50
Figure 6.1 Experimental setup .....	52
Figure 6.2 (a) Image from experiment with 0.25% intralipid. (b) Plot for image from with 0.05% intralipid.....	55
Figure 6.3 Images for different concentrations.....	56
Figure 6.4 Comparison of blue laser Bessel beam profiles after propagation through 0.1% to 0.2% intralipid solutions. Profiles using: Image intensity using (a) Blue intensity, (b) Gray intensity (c) Average red/blue/green (RBG) intensity .....	57
Figure 6.5 Experimental setup for self-healing property investigation .....	58
Figure 6.6 Images for 0.1% intralipid sample at different values of a.....	59
Figure 6.7 Comparison for 0.1% intralipid sample at different values of a.....	59
Figure 6.8 Images for 0.125% intralipid sample at different values of a.....	60
Figure 6.9 Comparison for 0.125% intralipid sample at different values of a.....	60
Figure 6.10 Image for 0.15% intralipid sample at different values of a. ....	61
Figure 6.11 Comparison for 0.15% intralipid sample at different values of a.....	61
Figure 6.12 Image for 0.175% intralipid sample at different values of a. ....	62
Figure 6.13 Comparison for 0.175% intralipid sample at different values of a.....	62
Figure 6.14 Image for 0.2% intralipid sample at different values of a. ....	63
Figure 6.15 Comparison for 0.2% intralipid sample at different values of a.....	63
Figure 7.1 Bessel function plot showing the FWHM and $1/e^2$ radii definitions.....	67

Figure 7.2 Bessel beam profile .....	68
Figure 7.3 0.1% intralipid experiment result .....	69
Figure 7.4 Simulation transmittance results for a Bessel beam of intralipid solutions.....	72
Figure 7.5 Experimental results for a Bessel beam of intralipid solutions .....	72
Figure 7.6 Total intensity from experiments and transmittance from simulation.....	73
Figure 7.7 Maximum intensity from experiments and transmittance from simulation ....	73
Figure 7.8 Comparison for 0.1% intralipid sample at different positions .....	76
Figure 7.9 Comparison for 0.125% intralipid sample at different positions .....	76
Figure 7.10 Comparison for 0.15% intralipid sample at different positions .....	77
Figure 7.11 Comparison for 0.175% intralipid sample at different positions .....	77
Figure 7.12 Comparison for 0.2% intralipid sample at different positions .....	78
Figure 7.13 Minimum reconstructive distance related to optical property .....	79

## Nomenclature

$a$	angle
$d$	obstacle size
$d_f$	fringe spacing
$d_r$	step size in radius dimension
$d_z$	step size in depth dimension
$d_a$	step size in angle dimension
$f$	focal length Bessel beam
$g$	scattering anisotropy
$k$	wave number $k = \frac{2\pi}{\lambda}$
$n$	index of refraction
$n_r$	number of steps in radius dimension
$n_z$	number of steps in depth dimension
$n_a$	number of steps in angle dimension
$r$	radius
$r_0$	spot radius for Bessel beam
$v$	volume
$z$	depth
$A$	relative specific absorption
$A(r,z)$	A as a function of r and z
$C_w$	weight concentration
$C_v$	volume concentration
$E$	electric field intensity

$F$	relative fluence, probability
$F(r,z)$	F as a function of r and z
$I$	photon intensity
$I_0$	photon initial intensity
$L_{re}$	minimum distance for the beam to reconstruct
$M$	mass
$N_a$	total number of absorbers in a unit volume
$N_s$	total number of scatterers in a unit volume
$P$	power
$Q_a$	absorption efficiency
$Q_s$	scattering efficiency
$R$	beam radius
$R_d$	relative diffuse reflectance
$R_d(r,a)$	$R_d$ as a function of r and a
$T_t$	relative diffuse transmittance
$T_t(r,a)$	$T_t$ as a function of r and a
$Z_{shadow}$	shadow zone length
$\alpha$	axicon base angle
$\beta$	beam deviation angle $\beta = (n-1) \alpha$
$\mu_a$	absorption coefficient
$\mu_s$	scattering coefficient
$\mu_s'$	reduced scattering coefficient $\mu_s' = \mu_s(1 - g)$
$\mu_t$	total interaction coefficient $\mu_t = \mu_a + \mu_s$

$\sigma_a'$	absorption cross-section
$\sigma_s'$	scattering cross-section
$\sigma_a$	geometry cross-section area of the absorber
$\sigma_s$	geometry cross-section area of the scatterer
$\lambda$	wavelength
$\rho$	specific weight
$\omega_0$	laser beam diameter
DOF	depth of field
MCML	Monte Carlo simulation program for multi-layered turbid media
CONV	MCML companion convolution program

# Chapter 1 Introduction

## 1.1 Background

Light tissue interaction studies have a variety of clinical applications such as skin treatment, phototherapy and laser surgery. Laser was invented during 1950's and there have been many studies about laser propagating in bio-tissue-like media [1] [2]. Most lasers produce an intensity profile with Gaussian distribution. In recent years, there has been significant interest in other intensity distributions such as Bessel and Airy beam distributions which have unique properties. Near-Bessel beams can be produced by an axicon, which is simply a conical lens [3].

Bessel beams, compared to Gaussian beams, have many advantages such as self reconstruction [4], long depth of field and non-diffraction. In the last 30 years, many studies have been published comparing different aspects of Gaussian and Bessel beams, such as their propagation after passing through an aperture [5], and their efficiencies of generation of optical harmonic [6].

One of the most interesting properties of Bessel beams is the self- reconstruction property which means that when a part of these beams is blocked, they reconstruct to the original profile as they propagate [4] [7] [8]. This property is also known as self-healing property of beams. Another beam having the self-healing property is the Airy beam [9].

The other important property of Bessel beams is non-diffraction [10]. Bessel beams are the most common known diffraction- free light beams. Another type of non-diffraction light beams is the Airy beams [9] [11]. According to this property, the light beam

intensity profile does not change over time or travel space, which is beneficial in terms of energy delivery. Many experiments [8] were conducted to prove the near non-diffraction property of Bessel beams.

The last important property of Bessel beams is that they have a long depth of field which is advantageous in different applications such as imaging [12]. As mentioned previously, Bessel beams are frequently generated by axicons. An axicon is a special type of optical lens which has a focal line instead of a focal point and the Bessel profile will be within the focal region. There are numbers of ways to modify the focal region, for example changing the base angle  $\alpha$  of the axicon [13] [14]. The three mentioned properties of Bessel beams can result in a much better energy delivery to the tissue [8].

According to the Monte Carlo method by Wang [15] [16], the software Monte Carlo modeling of light transport in multi-layered tissues (MCML) simulates the propagation of a pencil beam in tissue to create an impulse profile and the software convolution (CONV) convolves the impulse profile generated by MCML with certain types of beam intensity profile to approximate the propagation of beam in tissue.

Turbid media such as fat emulsions or Intralipid solutions are often used as phantoms for studying light propagation in bio-tissue. Many methods have been developed to measure the optical properties in these turbid media as well as other types of solutions [17] [18].

## 1.2 Objective

The purpose of this research is to investigate the propagation of Bessel beams in tissue and to compare it to that of Gaussian beams in terms of penetration. The Monte Carlo

method will be used to simulate this propagation. Experiments will also be conducted by generating a Bessel beam and allowing it to propagate in Intralipid solutions and measuring the resulting intensity profiles. Experiments will be used to access the validity and applicability of MCML. This is important since this software is widely used in spite that it does not take into account the wave behavior of the light.

### 1.3 Scope

The research project described in this thesis can be divided into three stages. In the first stage, we modified the CONV program into Matlab software and implemented the Bessel beam convolution about a pencil beam profile generated from the MCML. Then, we used the MCML [15] and CONV [16] programs to numerically simulate the propagation of Bessel and Gaussian beams in tissue. After the first stage, we used a blue laser and an axicon to generate a Bessel beam, which is allowed to propagate through several tissue-like phantoms (Intralipid solutions) with different concentrations. We used a CMOS camera to capture cross section images of the beam and develop Matlab programs to measure the intensity distributions from those images. At last, we compared the results from the experiments and simulations. Besides, we also conducted experiments investigating the self reconstructive properties of Bessel beam by observing the difference on the image while moving the intralipid sample between the camera and axicon.

The remainder of the thesis is organized as follows. Chapter 2 reviews the relevant literature to the subjects. The optical properties of tissue and their determinations are covered in chapter 3. The simulation methods and results are presented in chapter 4 and

chapter 5. In chapter 6, we describe the experimental technique and results. Finally, in chapter 7 we discuss the results and summarize the conclusions of this work.

## Chapter 2 Literature review

This chapter contains a review of the relevant investigations related to Bessel beam propagation in tissue-like phantoms. This review is divided into five sections, which respectively focus on tissue-like phantoms, optical properties, Bessel beams, numerical simulations and experimental investigations related to Bessel beam propagation in tissue-like phantoms.

### 2.1 Tissue-like phantoms

For most light-tissue interaction studies, the ideal material for media would be a living organism or at least a fresh tissue sample. However, such samples are not always available for research purposes. Instead of real life tissue sample, tissue equivalent phantoms or tissue-like phantoms are frequently used for these studies. The advantages of using tissue-like phantoms over real tissue phantoms include the fact that compared to real tissue, tissue equivalent phantoms are easier to preserve, less expensive, and it is easier to manipulate its optical properties and its state of matter (ideally semisolid) [19]. For light tissue interaction studies, the most important properties of the propagating medium samples are their scattering and absorption properties [20]. The recipe ingredients for preparing any tissue equivalent sample include the scatterer, the absorber and the solvent [19]. Many ingredients have been used for tissue equivalent phantoms such as  $\text{Al}_2\text{O}_3$  particles, silicon dioxide, intralipid, ink, blood, azide, penicillin, bovine serum, and fluorochromes [21] [22]. Three great examples of ingredients of tissue-like samples that represent scatterer, absorber and solvent respectively are intralipid solution [18], India ink [23] and polyvinyl alcohol (PVA) slime [24].

Intralipid is an emulsion of water and phospholipid micelles [18], which is often used as a tissue equivalent phantom in optical experiments because it has no strong absorption bands in the visible region of the electromagnetic spectrum and has easy adjustable scattering properties [17] [25]. India ink is composed of a variety of fine soot known as lampblack, which has been widely used for writing and printing. In the studies of tissue equivalent phantom, India ink is best known for its absorption property [23]. As a result, India ink, which is good for visualization, is often used as a pure absorber mixed with other solutions like the intralipid mentioned above. Another phantom used for light-tissue study is a soft deformable tissue based on polyvinyl alcohol (PVA) slime [24]. This type of phantom can have an arbitrary size and shape by containing the slime within a thin latex shell. The phantom can remain stable within three months. Similar to the Intralipid and India ink, other ingredients can be added to the PVA slime in order to control its optical performance like scattering and absorption.

With the three components mentioned above, namely intralipid, India ink and PVA, it is possible to fabricate phantoms that are capable of mimicking desired optical properties [19]. However, for recent tissue light interaction studies, intralipid solutions are mostly used [8] [26]-[27][28]. Therefore, in order to replicate and compare with other people's work, we use intralipid solutions in the present thesis.

## 2.2 Techniques to determine the optical properties of tissue-like samples

In numerical studies, propagating medium is represented by its optical properties [29]. The most important optical properties are absorption and scattering [30] [31]. However, for light propagations, refractive index and other physical parameters such as specific

weight or average particle size are also important factors [18] [25]. Many numerical and experimental methods were developed to determine these optical properties of tissue or tissue equivalent samples [18] [32]. As mentioned in the last section, in this research, the type of tissue sample we focus on is intralipid solution.

In general, the optical properties of any sample, such as the refractive index [33], the average scatterer size [25] and the attenuation coefficient  $\mu_t$  [17] can be obtained by experimental measurements. Even though it is very difficult to directly measure the value of the absorption coefficient  $\mu_a$  and the scattering coefficient  $\mu_s$  [18], one of them can be easily calculated by the other combined with  $\mu_t$  [20]. Since  $\mu_s$  can be determined by many well developed methods such as the Mie theory and the Rayleigh theory, a typical template for  $\mu_a$  determination involves experimentally measuring an optical term that can derive  $\mu_t$  via numerical models such as radiative transport equation (RTE) or diffusion theory [18] [25] [34], calculating  $\mu_s$  via Mie or Rayleigh theories which make use of the average scatterer size and the wavelength of the light source, and the coefficient  $\mu_a$  is then calculated based on  $\mu_t$  and  $\mu_s$ . For intralipid solutions, the particle size varies from the smallest particle which has about 25nm diameter to the larger particles having a diameter of few hundreds of nanometers [18]. Therefore, for studies requiring more precision, instead of using average particle size [25] and computing all scatterers as equal, each scattering event is calculated individually based on its particle size [18].

The whole determination process for one set of optical properties could take significant time and resources. So mostly, when the optical properties values are needed in studies, using existing data would be most efficient. However, like many other physical properties, optical properties are usually affected by many factors such as wavelength and particle

size. For tissue samples, many of measurements were generated from the bio-medical field [35]. On the other hand, for intralipid samples, existing data is not sufficient. As a solution, the results of optical properties under similar conditions are described by fitting functions [18].

### 2.3 Bessel beams and axicons

An axicon [36] is a lens that has a conical shape. Axicons are different from spherical lenses, they generate Bessel beams instead of Gaussian beams. The Bessel beam is named by its beam intensity profile. If a collimated laser beam passes through the axicon center, the intensity profile would be approximated by the square of a zero-order Bessel function of the first kind [10]. There are other ways to generate a Bessel beam, for example, a collimated light beam passing through an annular aperture followed by a converging lens [3]. Compared to Gaussian beams, Bessel beams have three characteristics which are non-diffractiveness [3] [5], long focal range and self-reconstruction, also called self-healing [4] [8]. All these properties suggest that a Bessel beam has a better performance in biomedical imaging. The long DOF can be practical for capturing clear image over a longer range. The non-diffractive and self-reconstructive properties imply that Bessel beams deliver better penetrations in tissues. There are other solutions, for example airy beams [9] [11], which also show non-diffractive and self-reconstructive properties. Also multi-beam laser have been used for better penetrations [2].

### 2.4 Simulation of light propagation in tissue

The purpose of a light-tissue interaction simulation is to estimate how the photon and tissue would affect each other during the propagation. A statistical method, the Monte

Carlo simulation, is frequently used for these simulations [20] [30] [31]. The final state of each photon after the propagation is presented by a probability distribution function.

Monte Carlo methods generally involve aggregating results by repeating the computation of the same numerical solution with inputs randomly generated response from a probability distribution over a defined domain. The most famous application using the Monte Carlo methods involves the determination of the value of  $\pi$  [37]. In tissue interaction studies, this process can be described as repeatedly launching individual photons into tissue and computing their trajectories based on absorption and scattering events they would encounter during the propagation then record the final status of all the photons spatial distributions over the tissue.

The use of Monte Carlo for light tissue interaction was first developed by B.C. Wilson in 1983 [30]. Since then, many studies of visible and near-infrared interaction with bio-tissue interaction were performed using this method [20] [31] [38] - [40]. The software Monte Carlo modeling of light transport in multi-layered tissues (MCML) developed by Wang in 1995 [15], is still widely used until today because it can be combined with convolution methods [16] to simulate the propagations of light with different intensity profiles. However, the traditional Monte Carlo simulations do not address the wave behaviors of light. Therefore, unscattered light simulations will not form the diffraction limited spot size correctly [41]. To address this issue, many studies were conducted over the last two decades [42] - [49]. In the most recent study, Hokr proposed to modify the initial distribution of the pulse and the behavior of the unscattered photons of MCML so it will describe propagating ballistic photons along trajectories predicted by Gaussian optics until they undergo an initial scattering event [41].

Besides Monte Carlo methods, radiative transfer equation (RET) can also be used to analyze light or other types of wave transportation in a certain medium [50] [51]. However, RTE is difficult to solve without approximations. The most common approximation that is catered to this need is the diffusion approximation [52]. Different from Monte Carlo simulations, this method is based on differential equation solving and does not require the large amount of simulations to get a statistical result. Therefore, the computational time for diffusion theory would be much smaller than Monte Carlo theory but the results can be less accurate due to approximations [20].

## 2.5 Experimental investigations of laser beams propagating in tissue-like medium

Compared to simulations, experimental investigations would represent the results more realistically. A general setup for light tissue interaction study usually involve a light source (laser), a set of optical elements to modify the beam diameter (telescope), a second set of optical elements to generate desire beam profile, a tissue-like phantom sample (intralipid solution) and a sensor to measure the intensities (CCD camera) for further analysis [8]. The purpose of this type of research is usually to compare the response of propagation between the target type of beams and a well known type of beams to prove the superior of the new found beam in specific terms such as penetration or energy distribution [8] [27]. During the last few decades, the most popular beams studied were the non-diffraction beams such as Bessel beams and Airy beams and the reference beam type is usually Gaussian beams [53] [54]. Non-diffraction beams also have unique self-reconstruction or self-healing property. In 1998, Bouchal and co-workers introduced their experiments that use a single obstacle to block the center of a Bessel beam and after a

reconstruction region, the intensity profile of the beam would reconstruct to Bessel distribution [4].

## Chapter 3 Optical and light scattering properties of tissue

This chapter includes theory and numerical calculations of the optical properties of tissue-like phantoms used in this thesis. It mostly focuses on the determination of scattering properties for the target phantom: intralipid solutions, which have low absorption properties.

### 3.1 Optical properties

The tissue optical properties required for the Monte Carlo simulation of light propagation in tissue are: the absorption coefficient  $\mu_a$ , the scattering coefficient  $\mu_s$ , the scattering anisotropy  $g$  and the index of refraction  $n$ . The thickness is also used to characterize the propagating media sample. In this section, we review the definitions of these properties and explain the methods used to determine these properties in our simulations as well as in the experiments.

#### 3.1.1 Optical properties' definitions

A propagating media is quantified by its optical properties. Each one of these properties effects the photon propagation in a different way, for example, the index of refraction  $n$  is the ratio of the speed of light in a certain medium to the speed of light in vacuum. This parameter is used in Snell's law to determine whether or not the photon bounce back when hitting a boundary. Other optical properties were used in this work include scattering properties and absorption properties.

Scattering events can be described as a phenomenon by which when any form of radiation or moving particles encounters an obstacle, it will be forced to change direction from its original trajectory. Scattering properties are quantified in terms of the scattering

coefficient  $\mu_s$  and the scattering anisotropy  $g$ . They represent the probability of a certain change of direction of a photon after a scattering event. Scattering of light by a spherical particle can be modeled by the Mie theory or the Rayleigh theory. The condition of using Rayleigh theory is that the particle size is much smaller than the wavelength. Since the particle size of intralipid solutions (average 444 nm [25]) is very close to the wavelength of the light source used in this research (473 nm), we will use Mie theory to calculate scattering properties in section 3.4.

The scattering anisotropy  $g$  is a measure of the amount forward direction retained after a single scattering event. It can be calculated by [20]

$$g = \langle \cos\theta \rangle \quad (3.1)$$

where  $\theta$  is the angle between original light trajectory and the light trajectory after the scattering event and the symbol  $\langle \rangle$  refers to averaging.

For a single scatterer, the scattering cross-section  $\sigma_s'$  is given by

$$\sigma_s' = Q_s \sigma_s \quad (3.2)$$

where  $Q_s$  is the scattering efficiency and  $\sigma_s$  is the geometry cross-sectional area of the scattering particle.

By considering all the scatterers in a unit volume, we have the scattering coefficient  $\mu_s$ .

$$\mu_s = \sum_{n=1}^{N_s} Q_s \sigma_s \quad (3.3)$$

where  $N_s$  is the total number of scatterers in a unit volume.

Other than scattering of light, we also track its energy transfer. Absorption property is used for simulating the energy drop resulting from beam propagation. Similar to the scattering coefficient, the absorption coefficient is calculated by

$$\mu_a = \sum_{n=1}^{N_a} Q_a \sigma_a \quad (3.4)$$

where  $N_a$  is the total number of absorbers in a unit volume,  $Q_a$  is the absorption efficiency and  $\sigma_a$  is the geometry cross-section area of the absorbing particle.

Combining  $\mu_a$  and  $\mu_s$ , we have another coefficient that indicates the probability of photon drop after passing through a unit volume which is called the extinction coefficient or the total interaction coefficient  $\mu_t$

$$\mu_t = \mu_s + \mu_a \quad (3.5)$$

### 3.1.2 Optical properties determination methods

For simulation, the values of the optical properties of different tissues are mostly taken from the literature. We are only calculating the optical properties of the intralipid samples that are used in our experiments.

From the work of Michels and co-authors [18], the determination of the optical properties of 10% intralipid is described by a set of fitting functions. Based on ingredients and concentration of the sample we are able to determine the scattering properties of the sample by using the Mie scattering theory. An example of this calculation will be presented in the next section. It should be mentioned that for diluted samples, i.e. for concentrations less than 10%, the fitting functions are no longer valid.

### 3.2 Optical properties determination for 10% intralipid

This section presents an example of calculating the optical properties of 10% intralipid for a wavelength of 473 nm using the fitting functions from [18]. The details of the calculation are included in Appendix A.

### 3.2.1 Index of refraction

The formulation for index of refraction  $n$  is provided by the IAPWS (International Association for the Properties of Water and Steam). However, for room temperature and wavelengths over 400 nm, one can use Cauchy equation (3.6), to calculate the refractive index

$$n(\lambda) = I + \frac{J}{\lambda^2} + \frac{K}{\lambda^4} \quad (3.6)$$

$I$ ,  $J$  and  $K$  are constants specified in Appendix A, where we find the indices of refraction  $n_{water}$  and  $n_{soy}$  for a wavelength  $\lambda = 473$  nm corresponding to the two main components of the solution. It is assumed that the solutions are thoroughly mixed and that the mixture is of constant composition. Therefore, the refractive index is assumed to be proportionally related to the volumes of the compositions of the mixture

$$n = \frac{n_1 v_1 + n_2 v_2}{v_1 + v_2} \quad (3.7)$$

where  $v_1$ ,  $v_2$  and  $n_1$ ,  $n_2$  are the volumes and indices of refraction respectively of the two components and  $n$  is the index of refraction of the mixture. We assume that the refractive indices of other components than water are all identical to those of soybean oil. Then we can divide the mixture into two compositions which are Soybean oil, glycerol and eggphospholipid as the first composition and water as the second composition. The volume for first composition is calculated by

$$v_1 = m_{soy} / \rho_{soy} + m_{Glycerol} / \rho_{Glycerol} + m_{egg} / \rho_{egg} \quad (3.8)$$

where  $m$  refers to the mass and  $\rho$  to the specific weight. The water, as the second composition, has a volume of  $v_2 = v_{total} - v_1$ .

### 3.2.2 Absorption coefficient

The fitting function for  $\mu_a$  is

$$\mu_a = \frac{a}{1 + e^{-\frac{\lambda - x_0}{b}}} \quad (3.9)$$

where  $\lambda$  is given in nm and  $\mu_a$  is obtained in  $\text{mm}^{-1}$ . The parameters are shown in Table 3.1.

Table 3.1 Coefficients for calculation of the absorption coefficient

	a	b	$x_0$
water	$3.066 \times 10^5$	54.13	$1.77 \times 10^3$
soy bean oil	$1.171 \times 10^5$	-36.59	$-3.21 \times 10^2$

The total absorption coefficient is calculated by the sum of the single absorbers multiplied by their volume concentrations

$$\mu_{a(tot)} = \sum_{i=1}^n \mu_a(i) \sigma_a(i) \quad (3.10)$$

The volume concentration of intralipid 10% is given by

$$C_v = \frac{c_w \rho_b}{c_w \rho_b + (1 - c_w) \rho_s} \quad (3.11)$$

where  $\rho_w$  and  $\rho_s$  are specific weights of water and soybean oil respectively,  $C_w$  is the weight concentration of the sample which is 10%.  $C_v$  is determined to be 10.8%. The total coefficient of intralipid 10% is then given by

$$\mu_{a(tot)} = (1 - C_v) \mu_{a(water)} + C_v \mu_{a(soy)} \quad (3.12)$$

### 3.2.3 Scattering anisotropy

The fitting function for  $g$  is

$$g(\lambda) = y_0 + a \lambda \quad (3.13)$$

The parameters are shown in Table 3.2.

Table 3.2 Coefficients for calculation of the Scattering anisotropy

	Lipovenoes 10%	Lipovenoes 20%	ClinOleic 20%	Intralipid 10%	Intralipid 20%	Intralipid 30%
$y_0$	1.075	1.085	1.070	1.018	1.090	1.066
$a$	$-6.079 \times 10^{-4}$	$-6.029 \times 10^{-4}$	$-6.369 \times 10^{-4}$	$-8.82 \times 10^{-4}$	$-6.812 \times 10^{-4}$	$-4.408 \times 10^{-4}$

### 3.2.4 Scattering coefficient

With the parameters shown in Table 3.3, the fitting function for  $\mu_s$  is

$$\mu_s = a \cdot \lambda^b \quad (3.14)$$

where  $\lambda$  is given in nm and  $\mu_s$  is obtained in  $\text{mm}^{-1}$ .

Table 3.3 Coefficients for calculation of the Scattering coefficient

	Lipovenoes 10%	Lipovenoes 20%	ClinOleic 20%	Intralipid 10%	Intralipid 20%	Intralipid 30%
$a$	$1.576 \times 10^8$	$3.116 \times 10^8$	$3.468 \times 10^8$	$4.857 \times 10^8$	$3.873 \times 10^8$	$2.645 \times 10^8$
$b$	-2.350	-2.337	-2.381	-2.644	-2.397	-2.199

All the above parameters are calculated in Appendix A, and the resulting optical properties of 10% intralipid are shown in Table 3.4.

Table 3.4 Optical properties of 10% intralipid under wavelength of 473nm

$n$	$\mu_a$ (/cm)	$g$	$\mu_s$ (/cm)
1.36	$4.3 \times 10^{-4}$	0.6	410

### 3.3 Optical properties of intralipid samples

This section describes the procedures for the optical properties calculations for our experimental samples. Because the concentration of the samples and the wavelength of

light source can both be different from existing literature, it is difficult to apply the published fitting functions to solve this problem. Therefore, a method that is suitable of calculating the optical properties under any wavelength and any ingredient is necessary. For known ingredients, it is not difficult to obtain the different parameters, such as, specific weight or index of refraction of the individual ingredient. On the other hand, Mie theory requires only those parameters and the particle size to calculate the scattering properties. In this case, we assume the particles in the samples are made of homogeneous and isotropic materials so that particle size will be equal to the average size which is 444 nm [25]. As for absorption coefficients, the fitting function from [18] can still be used.

### 3.3.1 Mie theory

The procedure of using Mie theory to calculate scattering properties of samples can be found in the literature, for example in [20]. In order to determine the scattering coefficient  $\mu_s$ , we need to start with calculating the scattering efficiency  $Q_s$  and scattering anisotropy  $g$  ( $g = \langle \cos\theta \rangle$ ). The formulas are given bellow.

$$Q_s = \frac{2}{x^2} \sum_{l=1}^{\infty} (2l+1) (|a_l|^2 + |b_l|^2) \quad (3.15)$$

$$g = \frac{4}{Q_s x^2} \sum_{l=1}^{\infty} \frac{l(l+2)}{l+1} \text{Re}(a_l a_{l+1}^* + b_l b_{l+1}^*) + \frac{2l+1}{l(l+1)} \text{Re}(a_l b_l^*) \quad (3.16)$$

where the size parameters  $x$  and  $y$  are given by

$$\begin{cases} x = kr \\ y = n_{rel} x \end{cases} \quad (3.17)$$

where  $k = 2\pi n_b / \lambda$ ,  $n_{rel} = n_s / n_b$  and  $r$  is the radius of the particle.

In equation 3.15 and 3.16,  $l$  is the order of the Bessel functions and the coefficients  $a_l$  and  $b_l$  are given by

$$\begin{cases} a_l = \frac{\psi_l'(y)\psi_l(x) - n_{rel}\psi_l(y)\psi_l'(x)}{\psi_l(y)\zeta_l(x) - n_{rel}\psi_l(y)\zeta_l'(x)} \\ b_l = \frac{n_{rel}\psi_l'(y)\psi_l(x) - \psi_l(y)\psi_l'(x)}{n_{rel}\psi_l(y)\zeta_l(x) - \psi_l(y)\zeta_l'(x)} \end{cases} \quad (3.18)$$

where the Riccati-Bessel functions are defined for a parameter  $z$  by

$$\psi_l(z) = z j_l(z) = \left(\frac{\pi z}{2}\right)^{\frac{1}{2}} J_{l+\frac{1}{2}}(z) \quad (3.19)$$

$$\zeta_l(z) = \psi_l(z) + i \chi_l(z) \quad (3.20)$$

$$\chi_l(z) = -z y_l(z) = \left(\frac{\pi z}{2}\right)^{\frac{1}{2}} Y_{l+\frac{1}{2}}(z) \quad (3.21)$$

where the denotations for Riccati-Bessel function are,

$l$	order
$j_l$	Spherical Bessel function first kind
$y_l$	Spherical Bessel function second kind
$J_l$	Bessel function first kind
$Y_l$	Bessel function second kind
$h^{(2)}$	Spherical Hankel function second kind
$H^{(2)}$	Hankel function second kind

note that

$$h_l^{(2)}(z) = j_l(z) - i y_l(z) \quad (3.22)$$

$$H_l^{(2)}(z) = J_l(z) - i Y_l(z) \quad (3.23)$$

then we have

$$\xi_l(z) = z h_l^{(2)}(z) = \left(\frac{\pi z}{2}\right)^{\frac{1}{2}} JH_{l+1/2}^{(2)}(z) \quad (3.24)$$

The scattering coefficient is given by

$$\mu_s = \sum_{n=1}^{N_s} Q_s \sigma_s \quad (3.25)$$

where  $\sigma_s$  is cross section area of the particle, and  $N_s$  is the particle number density. Because Mie theory assumes spherical particle shape, the cross section area can be calculated by  $\sigma_s = \pi r^2$ . The particle number  $N$  can be calculated by the weight of the composition over the weight of the particle  $N = M_c / M_s = C_w V_{tot} \rho_b / V_s \rho_s$ , where  $C_w$  is the weight concentration of the composition. For spherical particles, particle volume  $V_s = \frac{4}{3} \pi r^3$ . At last, the particle number density is given by  $N_s = N / V_{tot}$ . Therefore, we can write the formula of scattering coefficient as

$$\mu_s = \frac{C_w \rho_b}{\frac{4}{3} \pi r^3 \rho_s} Q_s \pi r^2 \quad (3.26)$$

### 3.3.2 Application of Mie theory

The necessary input arguments for equation 3.26 are wavelength  $\lambda$ , particle size, weight concentration  $C_w$ , specific weights  $\rho_s$  and  $\rho_b$ , and indices of refraction  $n_s$  and  $n_b$  of particle and back ground solvent. In other words, we can determine scattering properties based on these parameters by using the Mie theory.

For our experimental samples, the solvent is water and the scattering particle is soy bean oil. We can easily look up their specific weights and refractive indices. We set the particle size to 444 nm and wavelength to 473 nm. In summary, Table 3.5 shows the parameters of the experimental samples that are not related with their concentration.

Table 3.5 Parameters of the experimental samples

$\lambda$ (nm)	$d$ (nm)	$\rho_s$ (g/cm <sup>3</sup> )	$\rho_b$ (g/cm <sup>3</sup> )	$n_s$	$n_b$
473	444	0.92	1	1.48	1.34

Five different concentrations of intralipid sample were used in our experiment (0.1%, 0.125%, 0.15%, 0.175% and 0.2%). To apply Mie theory, we are using Matlab software from [55]. This software uses  $C_v$  (volume concentration) instead of  $C_w$ . So we convert  $C_w$  into  $C_v$  by equation 3.11. Then, using the software, we can easily obtain the values of scattering coefficients  $\mu_s$  and scattering anisotropy  $g$ .

### 3.3.3 Absorption coefficients

The absorption coefficients of the experimental samples can be calculated by the method from [18]. Substitute  $\mu_{a(water)} = 1.2037 \times 10^{-4}/\text{cm}$ ,  $\mu_{a(soy)} = 4.4096 \times 10^{-4}/\text{cm}$  and the volume concentration  $C_v$  into equation 3.12, we can obtain the values of absorption coefficients  $\mu_a$ .

### 3.3.4 Index of refraction

The index of refraction of samples can be calculated by the method from [18] as well applying equation 3.7. The values of  $v_1$  and  $v_2$  can be easily calculated using the calculated  $C_v$  values. And the indices of refraction are given in appendix A, where  $n_{water} = 1.34$  and  $n_{soy} = 1.48$ . Then we can easily calculate refractive indices of those five samples.

In summary, the optical properties of tissue samples are found in the literature [35] and shown in next chapter. The optical properties of intralipid samples are calculated by using Mie theory and the methods from [18] and shown in Table 3.6. As we can see, because the concentrations of the samples are very low, the refractive indices hardly vary and are very close to the  $n$  value of water and the absorption coefficients are extremely low compared to scattering properties.

Table 3.6 Optical properties of intralipid samples

$C_w$ (%)	$C_v$ (%)	$\mu_s$ (/cm)	$g$	$\mu_a$ (/cm)	$n$
0.1	0.109	11.7	0.8688	$1.2072 \times 10^{-4}$	1.3402
0.125	0.136	14.6	0.8688	$1.2081 \times 10^{-4}$	1.3402
0.15	0.163	17.5	0.8688	$1.2089 \times 10^{-4}$	1.3402
0.175	0.19	20.4	0.8688	$1.2098 \times 10^{-4}$	1.3403
0.2	0.217	23.3	0.8688	$1.2107 \times 10^{-4}$	1.3403

## **Chapter 4 Simulation techniques**

The Monte Carlo modeling technique is a numerical method to solve problems which are impossible or extremely hard to solve using a deterministic algorithm. This method uses a computational algorithm to repeatedly and randomly generate simulations that are as similar to real life scenarios as possible and record the results for each simulation. After a sufficient number of simulations, the solution of the problem is statistically estimated. Monte Carlo methods are especially powerful dealing with problems with random inputs and coupled degrees of freedom such as non-solid structure design.

### **4.1 Software**

In this research, we apply Monte Carlo method by using and modifying the MCML software [15] to simulate the propagations of pencil beams in tissue-like samples. MCML is a steady-state Monte Carlo simulation program for multi-layered turbid media with an infinitely narrow photon beam as the light source. Another program provided with the software is CONV [16], which is a convolution program using the MCML output results to convolve for variable beam profiles. The original CONV allows us to choose only Gaussian or top flat beam profiles. The software MCML, CONV and the Maetzler's MATLAB code for the Mie theory were downloaded from the website [55]. The original MCML and CONV programs were written in standard ANSI C, we re-wrote them in Matlab to be able to use the different available libraries, and we added the possibility of convolving Bessel beam profiles. The results are organized in 2-D matrices containing the probability distributions of absorption, reflectance, and transmittance events calculated at different locations in the samples and resulting from an incoming pencil

beam. Then the software CONV is used to convolve the MCML results for the Bessel or Gaussian beam profiles. Convolution is defined as an integral that expresses the amount of overlap of one function  $g$  as it is shifted over another function  $f$  [56]. The convolution of MCML results and beam profile simulate the propagations of Bessel or Gaussian beams in tissue-like samples.

#### 4.2 Algorithm

This section describes the software structure. The method of MCML is well described in [20]. The geometry used by MCML is shown in Figure 4.1. A cylindrical coordinate system is used for recording physical quantities of photons as a function of  $r$  and  $z$ . The step size and number of steps along  $r$ ,  $z$  and  $a$  direction are denoted by  $dr$ ,  $dz$ ,  $da$  and  $nr$ ,  $nz$ ,  $na$  respectively.

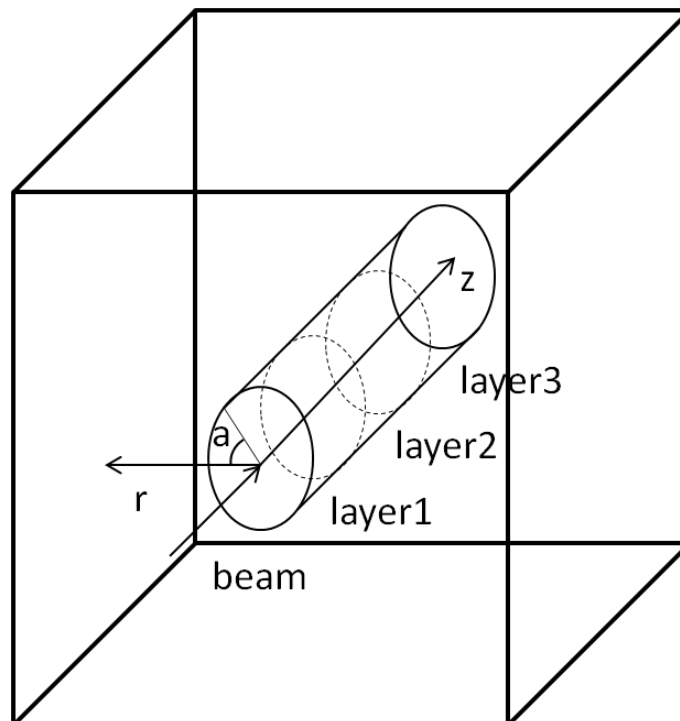


Figure 4.1 Schematic of beam tissue interaction modeled in MCML

The physical quantities are summarized in Table 4.1.

Table 4.1 Physical quantities to be computed in MCML

Symbol	Definition
$A(r,z)$	Relative specific absorption, probability of photon absorption by unit volume in the medium
$F(r,z)$	Relative fluence, probability of photon flow per unit area, can be computed by $A(r,z)$ and $\mu_a$
$R_d(r,\alpha)$	Relative diffuse reflectance, recording on the front surface
$T_d(r,\alpha)$	Relative diffuse transmittance, recording on the back surface

MCML is based on an algorithm adapted from [31] which is shown in Figure 4.2. The software simulates the beam propagation process by launching a number of photons and simulating each photon trajectory based on optical properties of the media and randomly generated factors such as, the spinning angle or the hopping distance of the photon after a scattering event, until there is a significant amount of simulations to demonstrate a realistic distribution of the reflectance, transmittance and absorption spatially over the medium area from the average events of all the photons.

More specifically, every time the software launches a photon, it initializes a set of parameters for the photon, such as an initial position and a unit direction vector which are both described in a Cartesian coordinate system and an initial weight which represents the total energy of the photon. Eventually the photon starts to propagate in the medium according to the scattering and absorption properties of the medium. During this propagation, the photon keeps dropping energy due to absorption. The software records

every absorption event according to the location of the event. At some point, the photon could encounter the boundary between different layers of the medium. Following the Snell's law, the software determines whether the photon passes through the boundary or bounce back to the current layer according to the indices of refraction of the layers. If the photon exits the last layer, the software records it as a transmission event. On the other hand, if the photon exits the first layer, the software records it as a reflection event. All the absorption, transmission and reflection events are recorded in a cylindrical coordinate system. Whenever a transmission, reflection or extinction happens, the software would launch another photon.

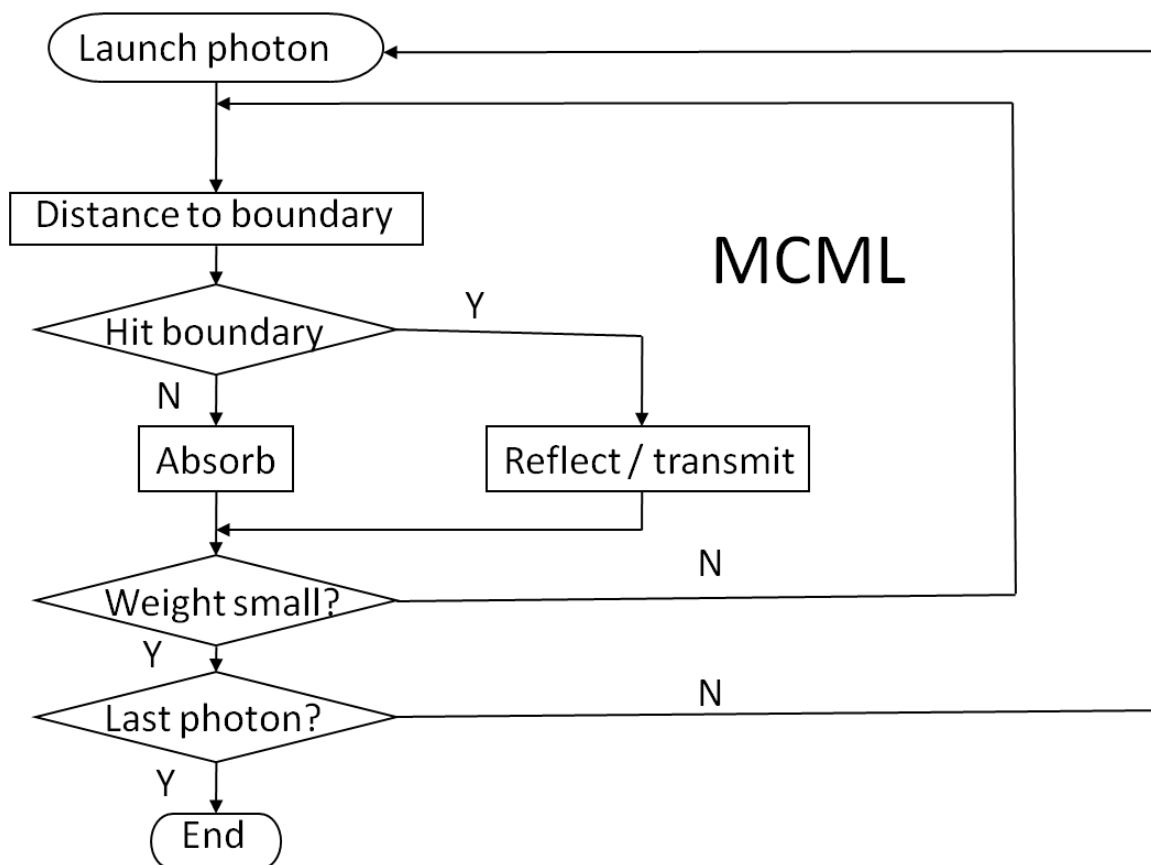


Figure 4.2 MCML algorithm (Adapted from [20])

The output of MCML follows the structure shown in Figure 4.3. By definition, the output files will be  $nr$  by  $nz+2$  matrices. The first row and last row represent the probability distributions of reflectance and transmittance events, and the probability distributions of absorption events are shown in between as  $nr$  by  $nz$  matrices.

Rd(1)	Rd(2)	.....	Rd(nr)
A(1,1)	A(1,2)	.....	A(1,nr)
A(2,1)	A(2,2)	.....	A(2,nr)
.....	.....	.....	.....
A(nz,1)	A(nz,2)	.....	A(nz,nr)
Tt(1)	Tt(2)	.....	Tt(nr)

Figure 4.3 MCML output

### 4.3 Methods

In this section we derive the convolution function we implemented into the CONV software. Since we are modifying the existing software, it is beneficial to keep the function in the same format as the Gaussian convolution function that exists in the software. Therefore, we follow the same procedure used in the determination of the Gaussian convolution from reference [20]. In the beginning we derive the beam profile equation from its field distribution. Then we determine the initial intensity which represents the constant part of the convolution function by relating the total power of the

laser and the intensity profile. At last, we substitute the initial intensity into the general form of convolution function to achieve the final convolution function for Bessel beams.

#### 4.3.1 Bessel beam profile

The electric field of a Bessel beam profile is given by [10]

$$E = \xi_B J_0(k\beta r) \quad (4.1)$$

where  $\xi_B$  is the amplitude at  $r = 0$ ,  $J_0$  is the zero-order Bessel function of the first kind.

The wave number  $k$  and the axicon refraction angle  $\beta$  are given by

$$k = \frac{2\pi}{\lambda} \quad (4.2)$$

$$\beta \approx (n - 1)\alpha \quad (4.3)$$

We substitute equation 4.3 into the intensity function (4.4) to obtain (4.5)

$$I = \frac{c}{2\pi} E \cdot E^T \quad (4.4)$$

$$I = \frac{c}{2\pi} \xi_B^2 J_0^2(k\beta r) \quad (4.5)$$

If we set  $I_0 = \frac{c}{2\pi} \xi_B^2$ , then equation 4.3 can be rewritten as

$$I = I_0 J_0^2(k\beta r) \quad (4.6)$$

#### 4.3.2 Initial intensity

By definition, the total power of the beam is equal to the integral of the beam intensity over the area

$$P = \int_0^\infty I \times 2\pi r dr = 2\pi I_0 \int_0^\infty r \times J_0^2(k\beta r) dr \quad (4.7)$$

According to [57], the part  $\int_0^\infty r \times J_0^2(k\beta r) dr$  can be calculated by

$$\int_0^\infty r \times J_0^2(k\beta r) dr = \frac{1}{2} r^2 (J_0^2(k\beta r) + J_1^2(k\beta r)) \Big|_0^\infty \quad (4.8)$$

And the part  $r^2(J_0^2(k\beta r) + J_1^2(k\beta r)) \Big|_0^\infty$  can be calculated by

$$r^2(J_0^2(k\beta r) + J_1^2(k\beta r)) \Big|_0^\infty = \lim_{R \rightarrow \infty} R^2 (J_0^2(k\beta R) + J_1^2(k\beta R)) \quad (4.9)$$

The series expansion at  $x = \infty$  of  $J_m(x)$  is given by [58]

$$\begin{aligned} J_m(x) = & \sin\left(\frac{\pi m}{2} - x + \frac{\pi}{4}\right) \left( \frac{(4m^2 - 1) \left(\frac{1}{x}\right)^{\frac{3}{2}}}{4\sqrt{2\pi}} + \frac{(-64m^6 + 540m^4 - 1036m^2 + 225) \left(\frac{1}{x}\right)^{\frac{7}{2}}}{1536\sqrt{2\pi}} + 0 \left(\left(\frac{1}{x}\right)^{\frac{11}{2}}\right) \right) \\ & + \cos\left(\frac{\pi m}{2} - x + \frac{\pi}{4}\right) \left( \sqrt{\frac{2}{\pi}} \sqrt{\frac{1}{x}} + \frac{(-16m^4 + 40m^2 - 9) \frac{1}{x}^{\frac{5}{2}}}{64\sqrt{2\pi}} \right. \\ & \left. + \frac{256m^8 - 5376m^6 + 31584m^4 - 51664m^2 + 11025}{49152\sqrt{2\pi}} + 0 \left(\left(\frac{1}{x}\right)^{\frac{11}{2}}\right) \right) \end{aligned}$$

Therefore, for large  $x$ :

$$J_m(x) \approx \sqrt{\frac{2}{\pi x}} \cos\left(x - \frac{(2m+1)\pi}{4}\right) \quad (4.10)$$

Then we can get

$$\frac{1}{2} \lim_{R \rightarrow \infty} R^2 (J_0^2(k\beta R) + J_1^2(k\beta R)) = \frac{R^2}{\pi k\beta R} \left( \cos^2\left(k\beta R - \frac{\pi}{4}\right) + \cos^2\left(k\beta R - \frac{3\pi}{4}\right) \right) \quad (4.11)$$

Because  $\cos(x) = -\sin\left(x - \frac{\pi}{2}\right)$ , we can have

$$\cos^2\left(k\beta R - \frac{\pi}{4}\right) + \cos^2\left(k\beta R - \frac{3\pi}{4}\right) = \cos^2\left(k\beta R - \frac{\pi}{4}\right) + \sin^2\left(k\beta R - \frac{\pi}{4}\right) = 1 \quad (4.12)$$

From equation 4.9 to 4.13, we can get

$$P = 2 \pi I_0 \frac{R}{\pi k \beta} = I_0 \frac{2R}{k \beta} \quad (4.13)$$

Therefore

$$I_0 = \frac{P k \beta}{2R} \quad (4.14)$$

Since we are doing finite width simulation, we set  $R$  to be ten times the beam radius.

### 4.3.3 Convolution

According to [20], the general form of a convolution in cylindrical coordinates is given

by

$$C(r, z) = \int_0^\infty G(r'', z) r'' \left( \int_0^{2\pi} S\left(\sqrt{r^2 + r''^2 - 2rr'' \cos \phi''}\right) d\phi'' \right) dr'' \quad (4.15)$$

where the notation  $r'' = r - r'$  and for  $S(r') = I_0 J_0^2(k\beta r')$ , we have

$$C(r, z) = \int_0^\infty G(r'', z) r'' \left( \int_0^{2\pi} I_0 J_0^2\left(k\beta \sqrt{r^2 + r''^2 - 2rr'' \cos \phi''}\right) d\phi'' \right) dr'' \quad (4.16)$$

where  $I_0 = \frac{P k \beta}{2R}$ . Therefore

$$C(r, z) = \frac{P k \beta}{2R} \int_0^\infty G(r'', z) r'' \left( \int_0^{2\pi} J_0^2\left(k\beta \sqrt{r^2 + r''^2 - 2rr'' \cos \phi''}\right) d\phi'' \right) dr'' \quad (4.17)$$

where equation 4.17 is the final convolution function. We implement it in to the program

CONV parallel to the Gaussian and top flat beam convolution functions to be the Bessel

beam convolution function.

## Chapter 5 Simulation results

This chapter presents the application of the software explained in last chapter to simulate Bessel and Gaussian beam interaction with different types of tissue. We firstly use MCML to simulate a pencil beam propagating in each sample, then use CONV to convolute the result with both Gaussian and Bessel beams. To demonstrate the capability of the program, we will show its performance with different types of phantoms. In section 5.1, we show the simulation results of single layered samples for four real tissue examples. The significant variance of the optical properties of these different types of tissue shows how they affect the simulation results. Section 5.2 on the other hand describes the simulation of two examples of multilayered samples which are an artery system and an integumentary system model. Section 5.3 demonstrates the simulations of different concentrations of intralipid solutions which will be used for comparison with the experimental results.

### 5.1 Single layer simulations

Four tissue samples are selected for testing the simulation program. The values of the optical properties of these samples are taken from [35], which are obtained through experiments using a red laser (wavelength 660 nm). We set the wavelength in our simulations to 660 nm in order to use these optical properties. Since we focus only on the effect of the optical properties on the simulation results, we keep the other parameters the same for all of these simulations. Therefore, the propagating media phantoms are modeled as the tissue samples being contained within a  $12.5 \times 12.5$  mm quartz cuvette which is later used in the experiments we conduct. The optical properties are shown in

Table 5.1. For the quartz cuvettes, we assume they are optically clear, meaning zero scattering and absorption properties. The refractive index of quartz is taken from [59].

Table 5.1 Tissue samples' optical properties (adapted from [35])

Tissue	Aorta	Blood	Dermis	Epidermis	Quartz
$n$	1.4	1.4	1.4	1.4	1.46
$\mu_a$ (/cm)	0.52	15.5	2.7	35	0
$\mu_s$ (/cm)	316	644.7	187.5	450	0
$g$	0.87	0.982	0.8	0.8	0

For every simulation, we start by presenting a table containing the input data needed. This constitutes a template for the MCML input profile. For example, a template for the simulation with Aorta is shown in Table 5.2.

Table 5.2 MCML input file template with aorta parameters

No. of photons	100000	layer	$n$	$\mu_a$ (/cm)	$\mu_s$ (/cm)	$g$	$d$ (cm)
$dz$ (cm)	0.03	1	1	Ambience above			
$dr$ (cm)	0.00004	2	1.46	NA			0.125
No. of $dz$	40	3	1.4	0.52	316	0.87	1
No. of $dr$	1000	4	1.46	NA			0.125
No. of $da$	1	5	1	Ambience below			

In Table 5.2, number of photons refers to the total number of photons launched. This number indicates the population of the simulation. The bigger the number is the more accurate the results are and the longer it takes to calculate. Through our simulations, we notice that once the number of photons reaches 100000, the results stop changing notably. Therefore, the computational time becomes priority. For sections 5.1 and 5.2, we set this number to 100000 so it will take approximately one minute to compute due to the large absorption values. For low concentrated intralipid samples, 100000 photons simulation

only takes seconds to compute. However, because of these samples' small optical properties, the probability of the light scattered over the whole scanning area is low, in fact, sometimes we don't have enough absorption events distributed over the medium area to make the impulse responses profile for convolution. Therefore we set the total number of photons to 1000000. The  $dz$  and  $dr$  parameters are the step sizes in the  $z$  and  $r$  directions respectively, and number of  $dz$ , number of  $dr$  and number of  $da$  are the number of steps in this simulation. As mentioned in the last chapter,  $r$  and  $z$  are radius and depth dimensions respectively. It is notable that  $nr$  is significantly larger than  $nz$ . That is because the most important output term transmittance doesn't include  $z$  dimension. The parameter  $a$  represents the angles dimension. Because of the axial symmetry of the system, we could set the number of  $da$  to 1 to eliminate angles dimension. This way, we are calculating the average values along the whole circles corresponding with every radius value. As a result, we will have a two dimensions result instead of a three dimensions results which is easier for further calculations in the CONV program. After the MCML simulation, the output file will be in the format that was shown in Figure 4.3.

After MCML, a 2-D array containing absorption  $A(r,z)$ , diffuse reflectance  $Rd(r,a)$ , and transmittance  $Tt(r,a)$  is obtained. The arrays MCML produces represent the impulse responses to be used in the CONV program to perform the convolution. In this part, the inputs that are needed for the software is the impulse responses and a beam profile which is shown in Table 5.3. In this table, the wavelength and axicon base angle parameters are used for calculating the beam radius for Bessel beam.

Table 5.3 Beam profile for CONV

Total energy (J)	Beam radius (cm) ( Gaussian or flat)	Beam type	Wavelength (nm)	Axicon base angle
1	0.0042	1, 2 or 3	660 nm	0.5 °

To make the results comparable, the total energy for the light source and the Gaussian beam radius are normalized to constants as shown above for all simulations in sections 5.1 and 5.2. Besides, all simulation results are normalized by total energy (summation of all values of  $Rd$ ,  $A$  and  $Tt$ ). The wavelength and the axicon base angle are used to determine the radius of Bessel beam (calculation will be described in chapter 7). The beam type parameter indicates the type of beam that is convoluting with the MCML output file. Three beam types built in the CONV are top flat beam, Gaussian beam and Bessel beam, which are denoted by 1, 2 and 3 respectively.

#### 5.1.1 Simulation with Aorta sample

The optical properties for the aorta sample were shown in Table 5.2. As mentioned before, it's assumed that the tissue sample is placed in the cuvette. The results of Gaussian beam convolution are shown in figure 5.1- 5.4.

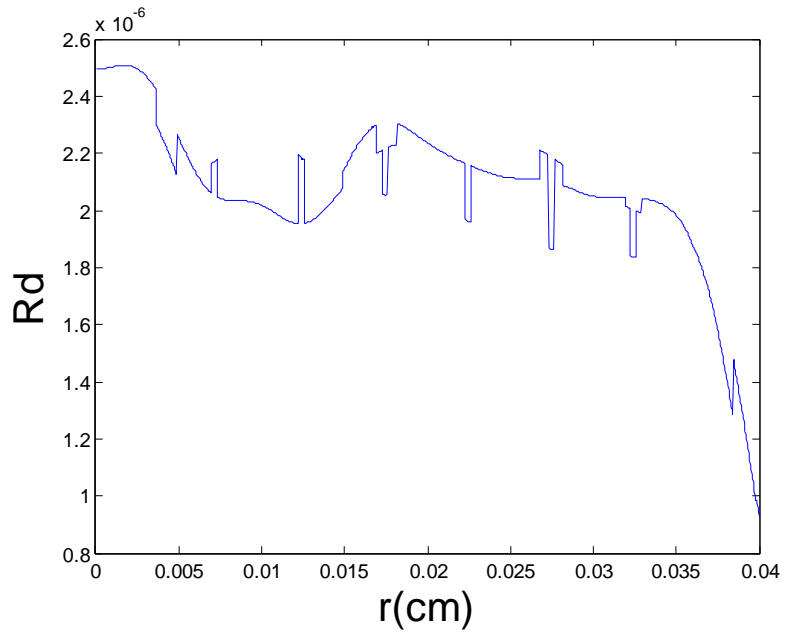


Figure 5.1 Diffuse reflectance for a Gaussian beam ( $r=0.0042$ cm) (Aorta)

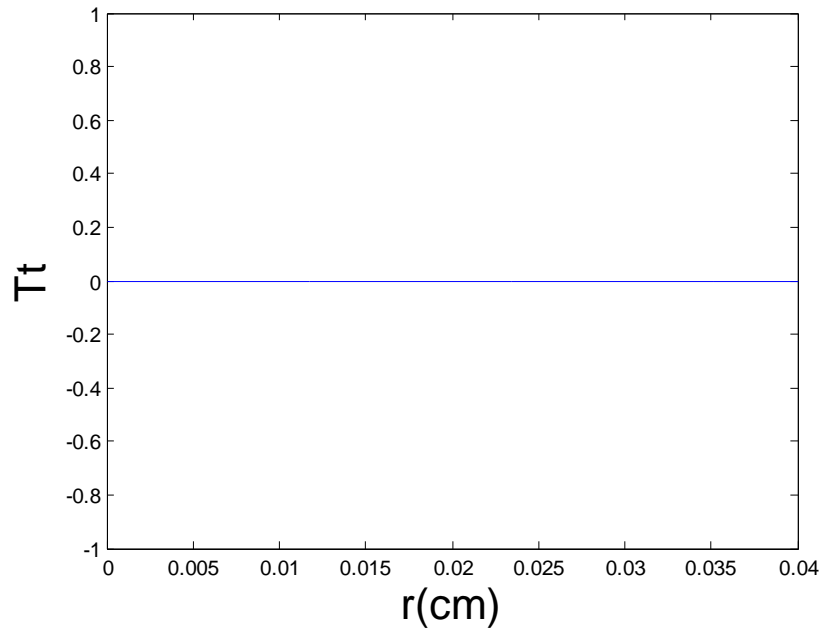


Figure 5.2 Transmittance for a Gaussian beam ( $r=0.0042$ cm) (Aorta)

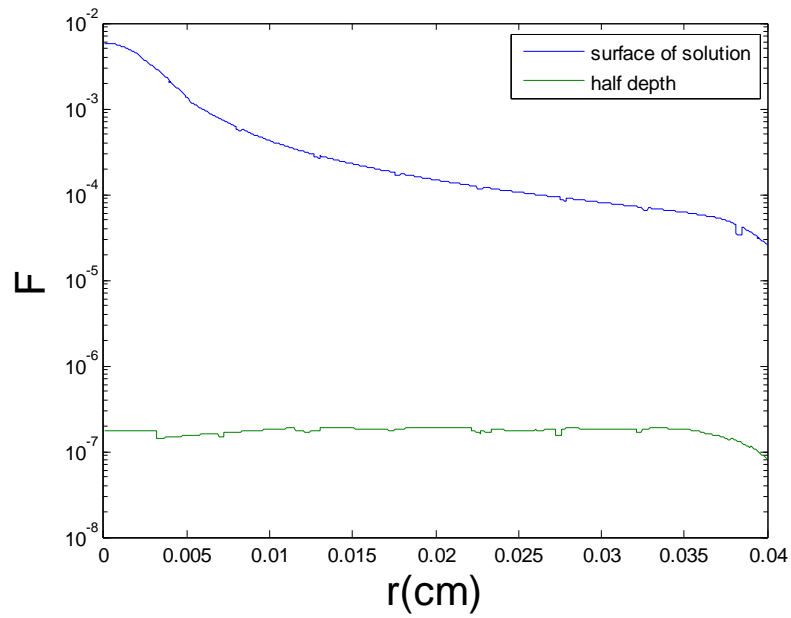


Figure 5.3 Fluence at surface and half depth of the sample layer for a Gaussian beam  
( $r=0.0042\text{cm}$ ) (Aorta)

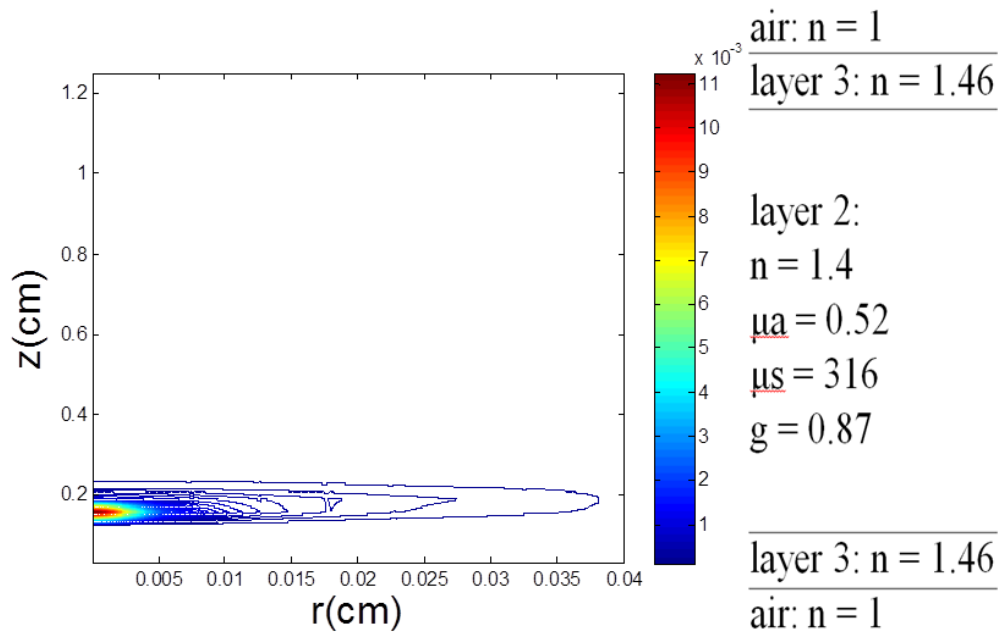


Figure 5.4 Contour plot of the fluence for a Gaussian beam ( $r=0.0042\text{cm}$ ) (Aorta)

The distributions of diffuse reflectance, transmittance and absorption are shown in Figure 5.1, Figure 5.2 and Figure 5.3. In Figure 5.2, we can see that the transmittance is practically equal to zero. That is because light can't penetrate one centimetre tissue sample with this configuration. In Figure 5.3 and Figure 5.4, the term fluence is defined as the local absorption normalized by the local absorption coefficient. If the media has uniform absorption coefficient, we have

$$F(r,z) = A(r,z) / \mu_a \quad (5.1)$$

where  $F(r,z)$  is the local fluence,  $A(r,z)$  is the local absorption and  $\mu_a$  is the absorption coefficient.

Because  $A(r,z)$  is a 2-D array, we will have to use a 2-D plot method like contour plot to represent the full distribution of this parameter. A contour plot of fluence with corresponsive layer detail on the side is shown in Figure 5.4. However, we can still plot 2 lines from this 2-D array from different location to see the difference like we showed in Figure 5.3. In order to do so, we set the program to always return the values at the beginning of the sample layer and the middle of the sample layer. In some cases, because the photons couldn't pass through half of the layer, we can only see the blue curve which represents the value at the beginning of the sample layer.

For Bessel beam convolutions, simply switch the beam type from Gaussian beam (2) to Bessel beam (3), following the same procedure, we can plot the results from Bessel beam simulation. The results are combined with Gaussian beam simulation results as shown in Figure 5.5.

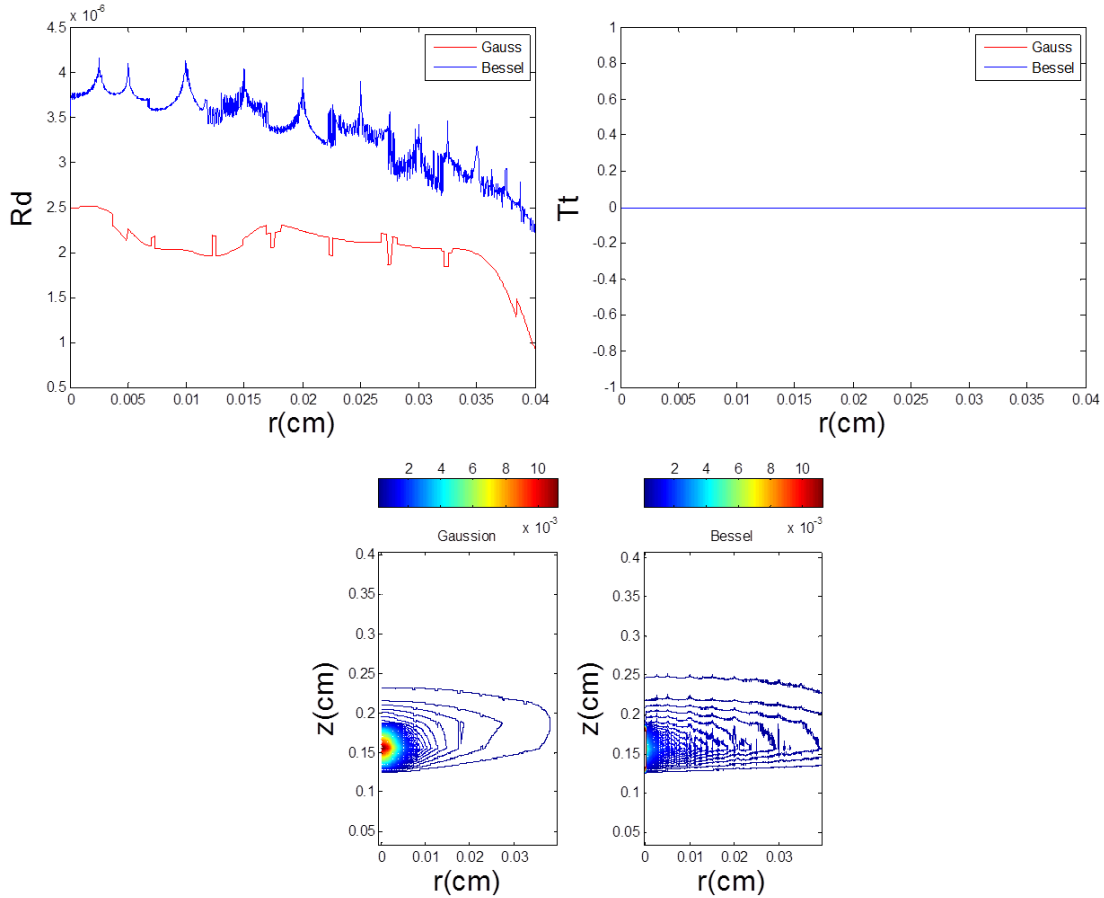


Figure 5.5 Arota simulation results comparison: reflectance, transmittance and fluence

In Figure 5.5, the results show that the Gaussian beam propagation has more energy absorbed by the sample and less energy exit the sample, which could suggest the Bessel beam has better resistance to absorption.

### 5.1.2 Simulation with blood sample

In this section, we repeat the same procedures to simulate the beam propagations in blood sample. We present the input file and the results figures following the order of the example shown in last section. The transmittance figure is not shown in this section since the value is still zero.

Table 5.4 MCML input file for blood sample

No. of photons	100000	layer	$n$	$\mu_a$ (/cm)	$\mu_s$ (/cm)	$g$	$d$ (cm)
$dz$ (cm)	0.03	1	1	Ambience above			
$dr$ (cm)	0.0004	2	1.46	NA			
No. of $dz$	40	3	1.4	15.5	644.7	0.982	1
No. of $dr$	1000	4	1.46	NA			
No. of $da$	1	5	1	Ambience below			

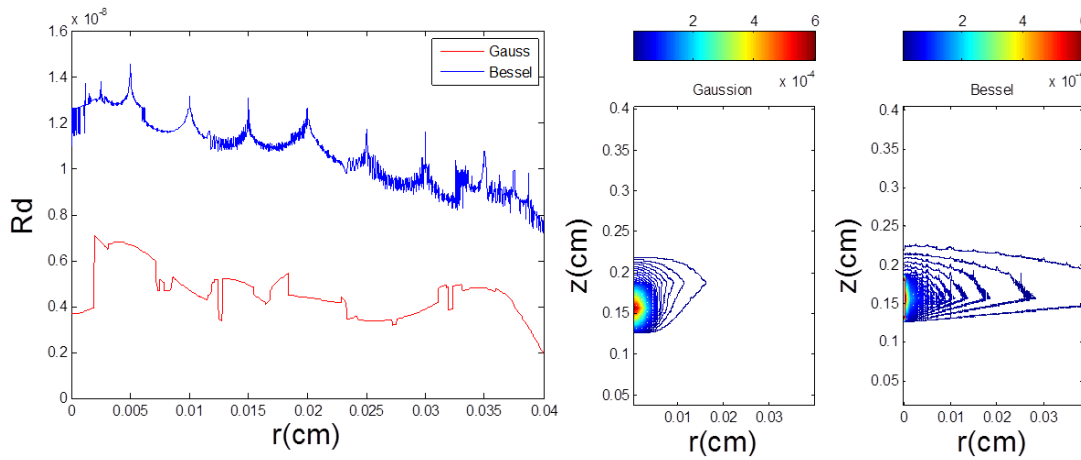


Figure 5.6 Blood simulation results comparison reflectance and fluence

The absorption coefficient of blood sample is considerably higher than aorta sample. From the results, we can see that the difference in diffuse reflectance from blood simulation is greater than it is in the aorta simulation, which further proves that Bessel beam resists absorption better than Gaussian beam.

### 5.1.3 Simulation with epidermis sample

Figure 5.5 and Figure 5.6 suggest that the average diffuse reflectance is lower when the absorption coefficient is higher, meaning a higher  $\mu_a$  results in the energy distributed more toward absorption. A simulation with the epidermis sample, which has an even higher absorption coefficient, is needed to test this hypothesis.

Table 5.5 MCML input file for epidermis sample

No. of photons	100000	layer	$n$	$\mu_a$ (/cm)	$\mu_s$ (/cm)	$g$	$d$ (cm)
$dz$ (cm)	0.03	1	1	Ambience above			
$dr$ (cm)	0.00004	2	1.46	NA			0.125
No. of $dz$	40	3	1.4	35	450	0.8	1
No. of $dr$	1000	4	1.46	NA			0.125
No. of $da$	1	5	1	Ambience below			

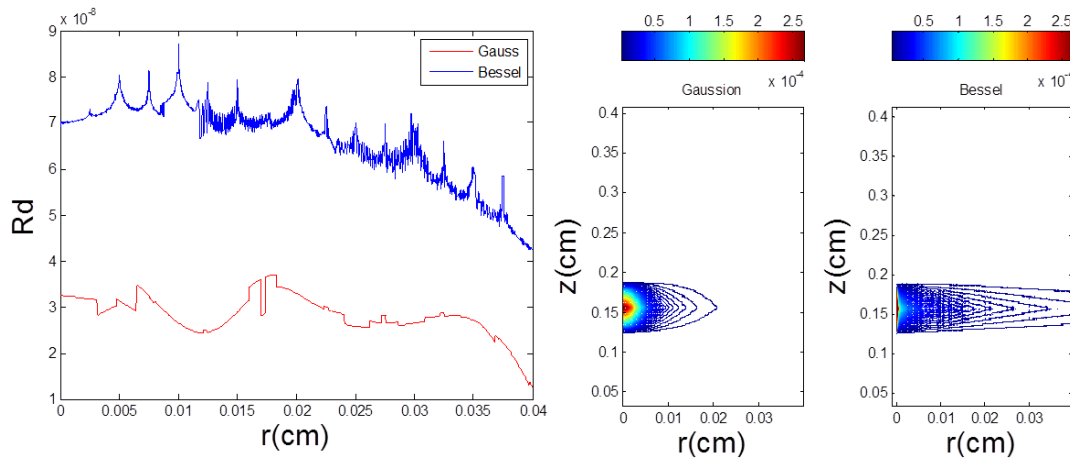


Figure 5.7 Epidermis simulation results comparison reflectance and fluence

The result is diffuse reflectance in this simulation is not lower than that of the blood sample as expected. However,  $R_d$  from simulations with epidermis sample is relatively close to that of blood sample than that of aorta sample. The inconsistency might be due to statistical error in the Monte Carlo method.

#### 5.1.4 Simulation with dermis sample

Since transmittance for these simulations is close to zero, the ratio of  $\mu_s / \mu_a$  is important in term of energy distribution. This ratio is roughly equal to 42, 70 and 600 for the blood, the dermis and the aorta samples respectively.

Table 5.6 MCML input file for dermis sample

No. of photons	100000	layer	$n$	$\mu_a$ (/cm)	$\mu_s$ (/cm)	$g$	$d$ (cm)
$dz$ (cm)	0.03	1	1	Ambience above			
$dr$ (cm)	0.00004	2	1.46	NA			0.125
No. of $dz$	40	3	1.4	2.7	187.5	0.8	1
No. of $dr$	1000	4	1.46	NA			0.125
No. of $da$	1	5	1	Ambience below			

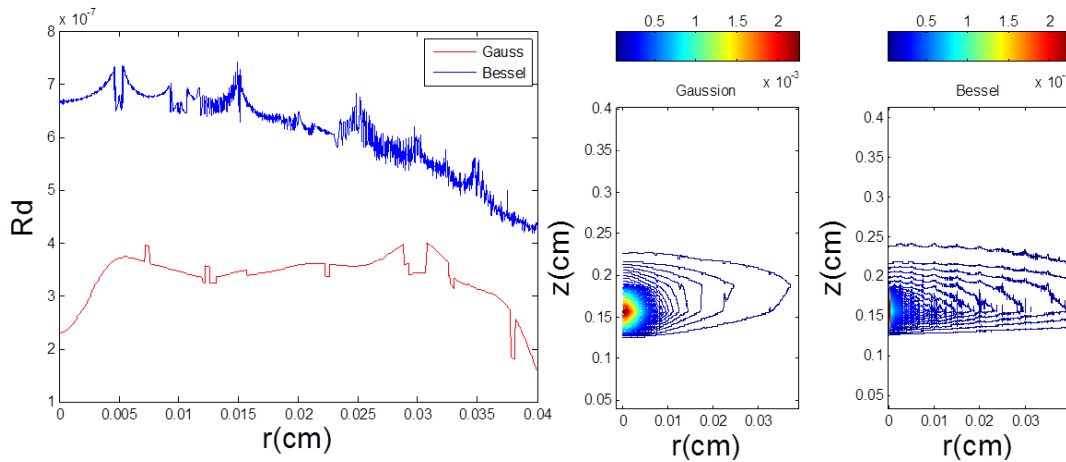


Figure 5.8 Dermis simulation results comparison reflectance and fluence

The reflectance from the aorta, which has a higher  $\mu_s / \mu_a$ , is much higher than that of dermis and blood. This is due to the fact that more photons are scattered and eventually escape from the surface.

## 5.2 Multilayered simulations

In this section, we simulated two multilayered samples modeling more realistic tissue configurations of artery and skin samples, which are shown in Figure 5.9. The software MCML is designed for medium with many layers. What differentiates the multilayered samples from the single layered samples is the numbers of layers that contain scattering or absorption properties. For example, the artery system sample has three main layers

which all contain optical properties. In this case, through the simulation, we can visually see the phenomenon when the light penetrates between layers with different optical densities.

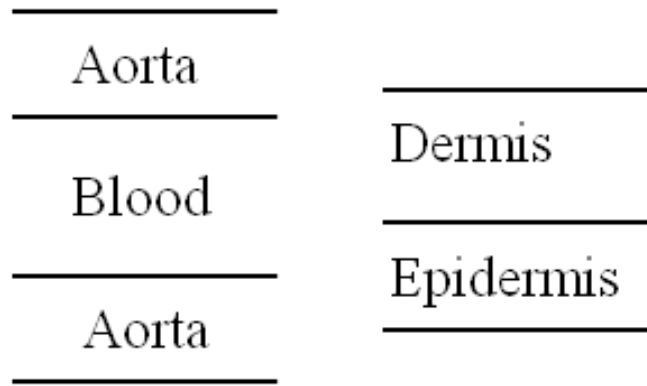


Figure 5.9 Artery system and Integumentary system models

### 5.2.1 Artery system simulation

Following the procedure from the last section, we start with the input files. The parameters for artery sample are shown in Table 5.7. The diameter and thickness of a carotid artery are provided by [60]. The simulation results are shown below in Figure 5.10.

Table 5.7 MCML input file for artery sample

No. of photons	100000	layer	$n$	$\mu_a$ (/cm)	$\mu_s$ (/cm)	$g$	$d$ (cm)
$dz$ (cm)	0.03	1	1	Ambience above			
$dr$ (cm)	0.00004	2	1.4	0.52	316	0.87	0.06
No. of $dz$	40	3	1.4	15.5	644.7	0.982	0.8
No. of $dr$	1000	4	1.4	0.52	316	0.87	0.06
No. of $da$	1	5	1	Ambience below			

From the results in Figure 5.10, we can see that most of the energy was absorbed by the first layer of the aorta wall. Meaning there was hardly any propagation of light in the

rest of the sample. So this simulation did not achieve the purpose of multi-layered simulation.

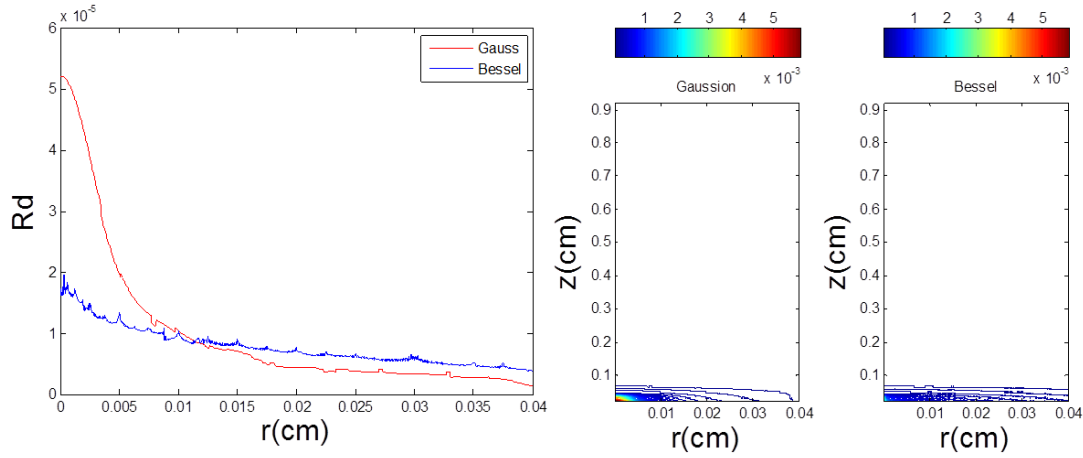


Figure 5.10 Artery simulation results comparison reflectance and fluence

### 5.2.2 Integumentary system simulation

The parameters for Integumentary system sample are shown in Table 5.8. The value of the thickness of the layers can be found on [61]. The simulation results are shown below in Figure 5.11.

Table 5.8 MCML input file for skin sample

No. of photons	100000	layer	$n$	$\mu_a$ (/cm)	$\mu_s$ (/cm)	$g$	$d$ (cm)
$dz$ (cm)	0.005	1	1	Ambience above			
$dr$ (cm)	0.00004	2	1.4	2.7	187.5	0.8	0.02
No. of $dz$	40	3	1.4	35	450	0.8	0.15
No. of $dr$	1000	4	1	Ambience below			
No. of $da$	1	5					

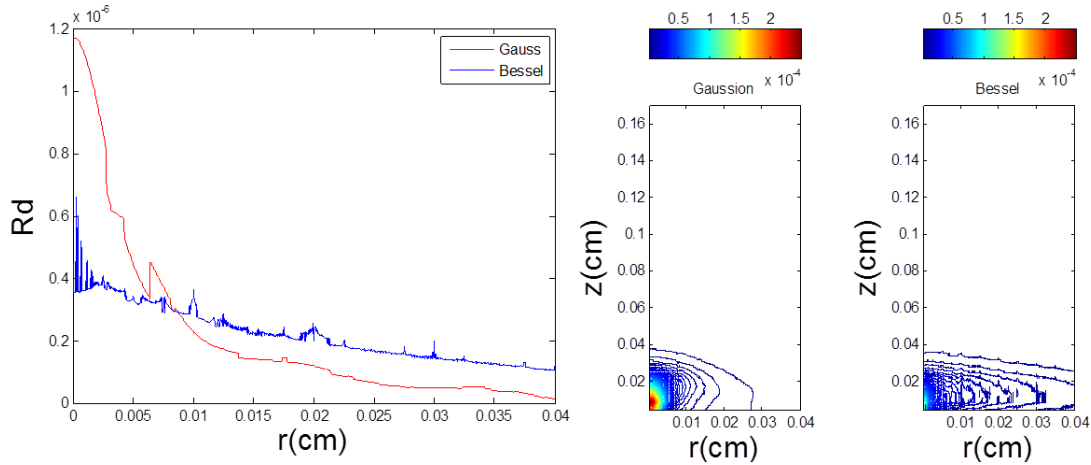


Figure 5.11 Skin simulation results comparison: reflectance and fluence

This example perfectly shows different optical densities of media effect the beam propagations. From the fluence contour plot in Figure 5.11, we can see both beams propagated better in the first 0.02 cm which is the dermis layer with low optical density. After the first layer, both propagations were terminated in a relatively short distance. Also, the intensity of Bessel beam propagation is much better concentrated to the center than that of the Gaussian beam.

### 5.3 Intralipid simulations

In this section, following the same procedures, we will simulate both Gaussian and Bessel beam propagations passing through five intralipid solutions with different concentrations. The concentrations of the samples are 0.1%, 0.125%, 0.15%, 0.175% and 0.2%. The optical properties of these samples were all calculated using the Mie theory mentioned in section 3.3. As mentioned in previous chapters, intralipid solutions are most commonly used as substitutes for tissue samples in light propagating studies. They are

easily acquirable and can be stored and preserved. Therefore, intralipid solutions are the best choice for us to be the experimental propagating media samples.

The purpose of the simulations that are described in this section is mostly to compare with the experimental result obtained in the lab which will be detailed in Chapter 6. In order to make the simulation results and experimental results comparable, we need to set the radius of simulations close to the scanning area radius in the experiments which is 0.04 cm (see Chapter 6). We determine the Bessel beam radius to be 0.003 cm (see chapter 7 for calculation), so that we set the Gaussian beam radius to be the same. And the step size to be much smaller than the Bessel beam radius (0.00004 cm). Two axicons, of base angles  $\alpha = 5^\circ$  and  $0.5^\circ$ , were available to generate the Bessel beam. For the experiments, we chose a  $0.5^\circ$  axicon for its longer focal range instead of the  $5^\circ$  axicon. Besides, the laser we use here is a blue laser with a wavelength of 473 nm. Then we represent the MCML input files and results for each simulations separately. So that we have the beam profile for this part of simulations shown below in Table 5.9. For the simulations for every sample we compare the distributions of transmittances from Gaussian and Bessel beams.

Table 5.9 Inputs profile for CONV

Total energy (J)	Beam radius(cm)	Beam type	Wavelength (nm)	Base angle (degree)
1	0.003	2 or 3	473	0.5

The input files for the 0.1% to 0.2% intralipid solutions are shown in tables 5.10 to 5.14 respectively. The results of the simulations for all solutions are shown in figures 5.12 to 5.16.

Table 5.10 MCML input file for intralipid 0.1% sample

No. of photons	1000000	layer	$n$	$\mu_a$ (/cm)	$\mu_s$ (/cm)	$g$	$d$ (cm)
$dz$ (cm)	0.03	1	1	Ambience above			
$dr$ (cm)	0.00004	2	1.46	NA			0.125
No. of $dz$	40	3	1.3402	1.2072e-4	11.7	0.8688	1
No. of $dr$	1000	4	1.46	NA			0.125
No. of $da$	1	5	1	Ambience below			

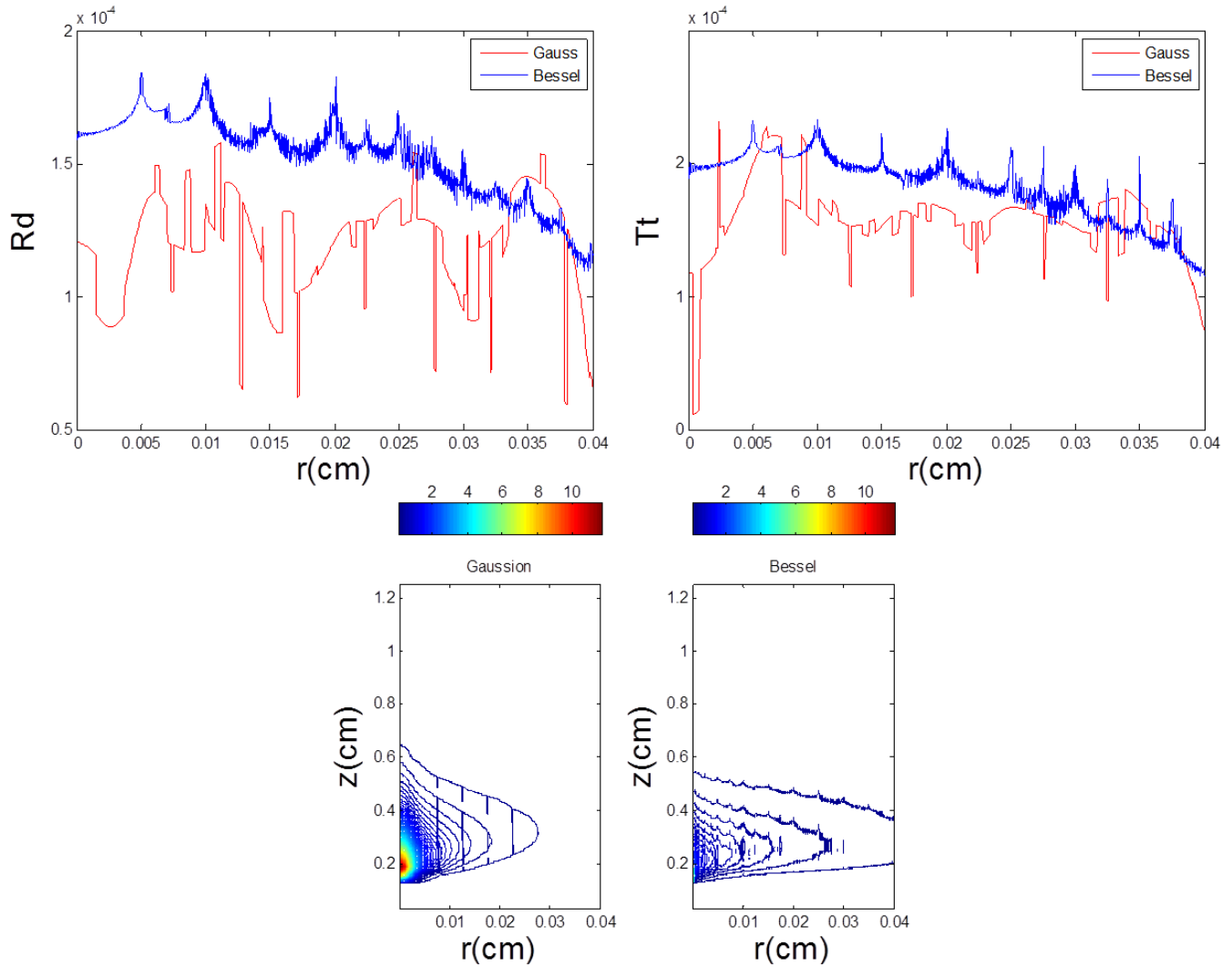


Figure 5.12 0.1% intralipid simulation results comparison: reflectance, transmittance and fluence

Table 5.11 MCML input file for intralipid 0.125% sample

No. of photons	1000000	layer	$n$	$\mu_a$ (/cm)	$\mu_s$ (/cm)	$g$	$d$ (cm)
$dz$ (cm)	0.03	1	1	Ambience above			
$dr$ (cm)	0.00004	2	1.46	NA			0.125
No. of $dz$	40	3	1.3402	1.2081e-4	14.6	0.8688	1
No. of $dr$	1000	4	1.46	NA			0.125
No. of $da$	1	5	1	Ambience below			

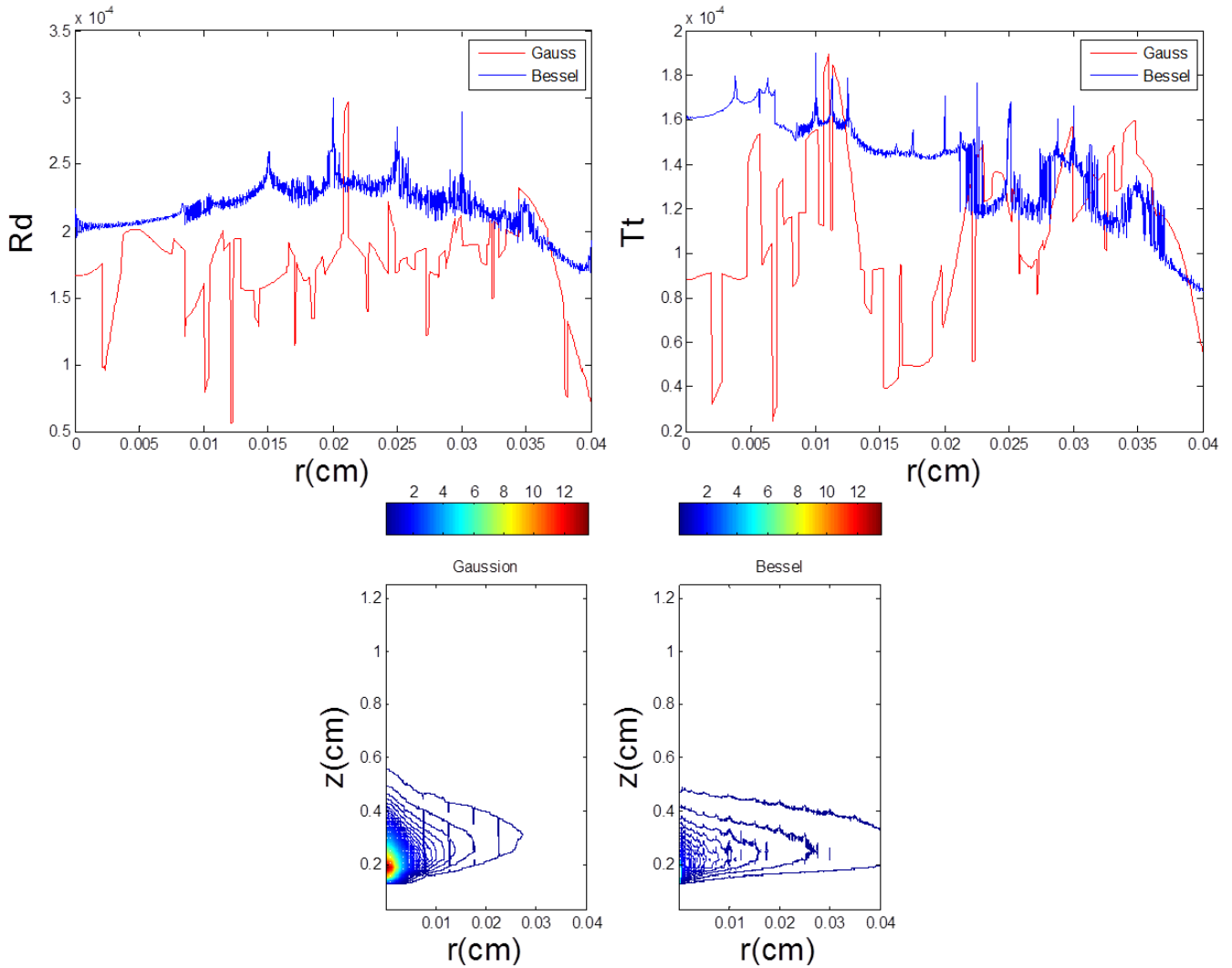


Figure 5.13 0.125% intralipid simulation results comparison: reflectance, transmittance and fluence

Table 5.12 MCML input file for intralipid 0.15% sample

No. of photons	1000000	layer	$n$	$\mu_a$ (/cm)	$\mu_s$ (/cm)	$g$	$d$ (cm)
$dz$ (cm)	0.03	1	1	Ambience above			
$dr$ (cm)	0.00004	2	1.46	NA			0.125
No. of $dz$	40	3	1.3402	1.2089e-4	17.5	0.8688	1
No. of $dr$	1000	4	1.46	NA			0.125
No. of $da$	1	5	1	Ambience below			

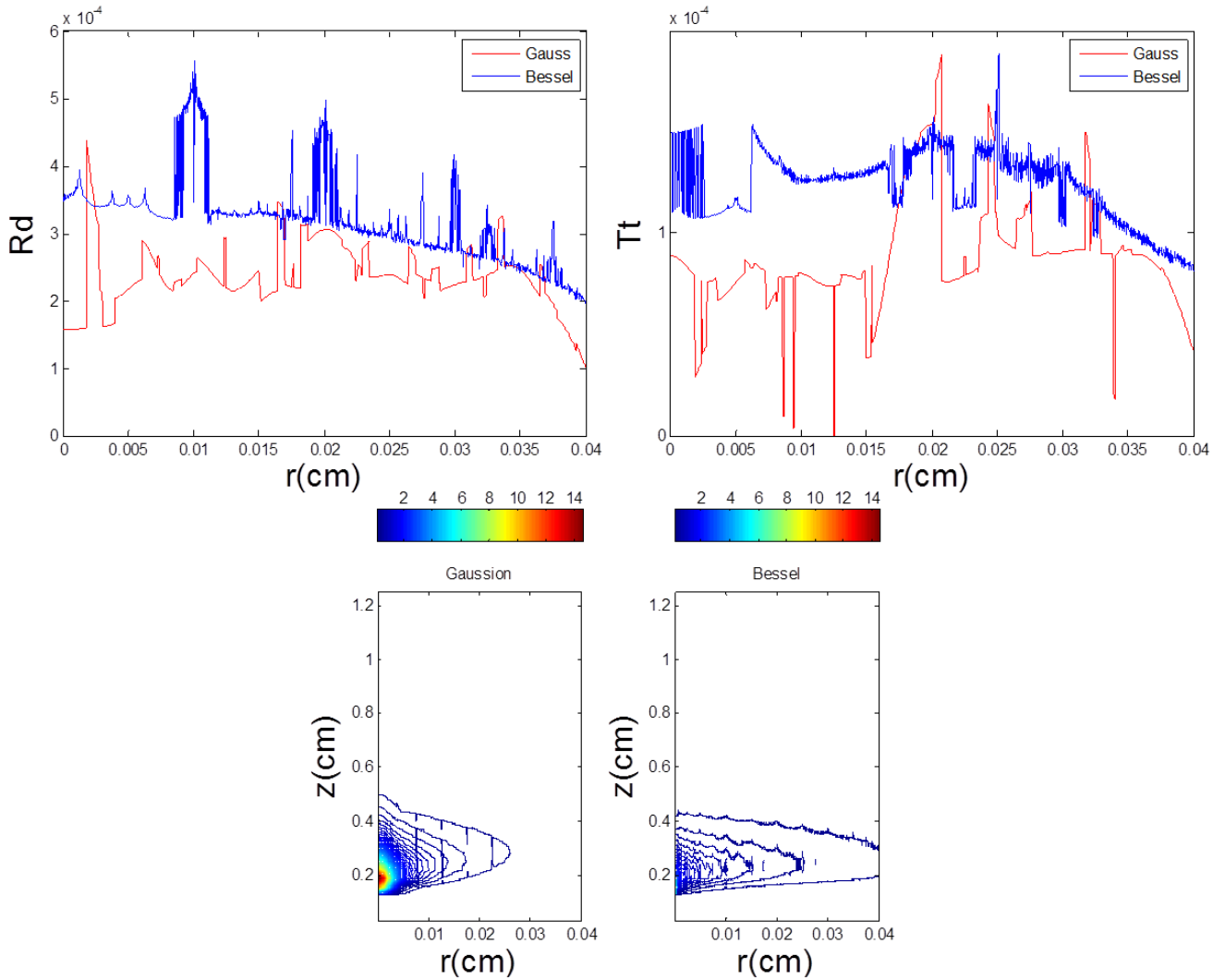


Figure 5.14 0.15% intralipid simulation results comparison: reflectance, transmittance and fluence

Table 5.13 MCML input file for intralipid 0.175% sample

No. of photons	1000000	layer	$n$	$\mu_a$ (/cm)	$\mu_s$ (/cm)	$g$	$d$ (cm)
$dz$ (cm)	0.03	1	1	Ambience above			
$dr$ (cm)	0.00004	2	1.46	NA			0.125
No. of $dz$	40	3	1.3403	1.2098e-4	20.4	0.8688	1
No. of $dr$	1000	4	1.46	NA			0.125
No. of $da$	1	5	1	Ambience below			

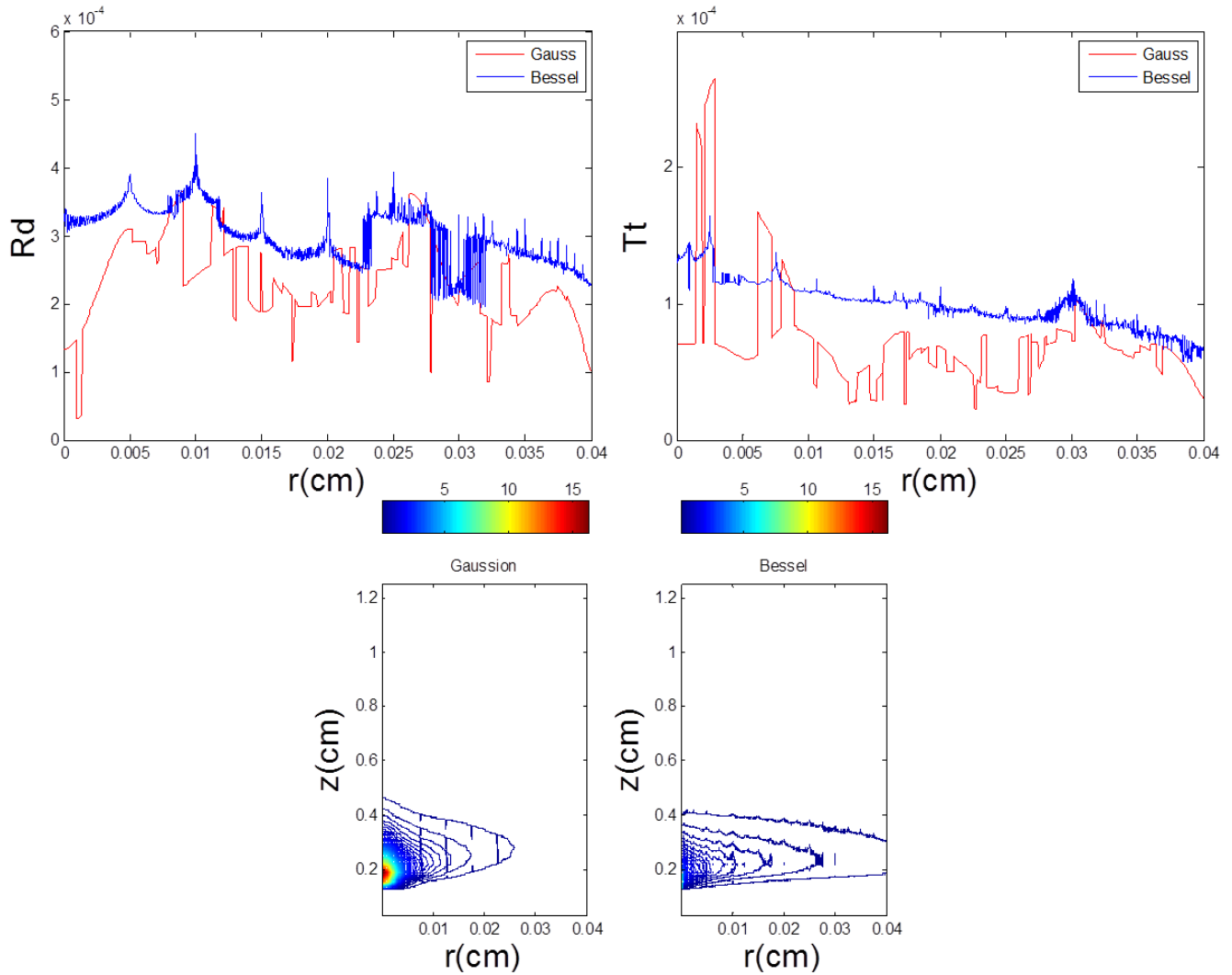


Figure 5.15 0.175% intralipid simulation results comparison: reflectance, transmittance and fluence

Table 5.14 MCML input file for intralipid 0.2% sample

No. of photons	1000000	layer	$n$	$\mu_a$ (/cm)	$\mu_s$ (/cm)	$g$	$d$ (cm)
$dz$ (cm)	0.03	1	1	Ambience above			
$dr$ (cm)	0.00004	2	1.46	NA			0.125
No. of $dz$	40	3	1.3403	1.2107e-4	23.3	0.8688	1
No. of $dr$	1000	4	1.46	NA			0.125
No. of $da$	1	5	1	Ambience below			

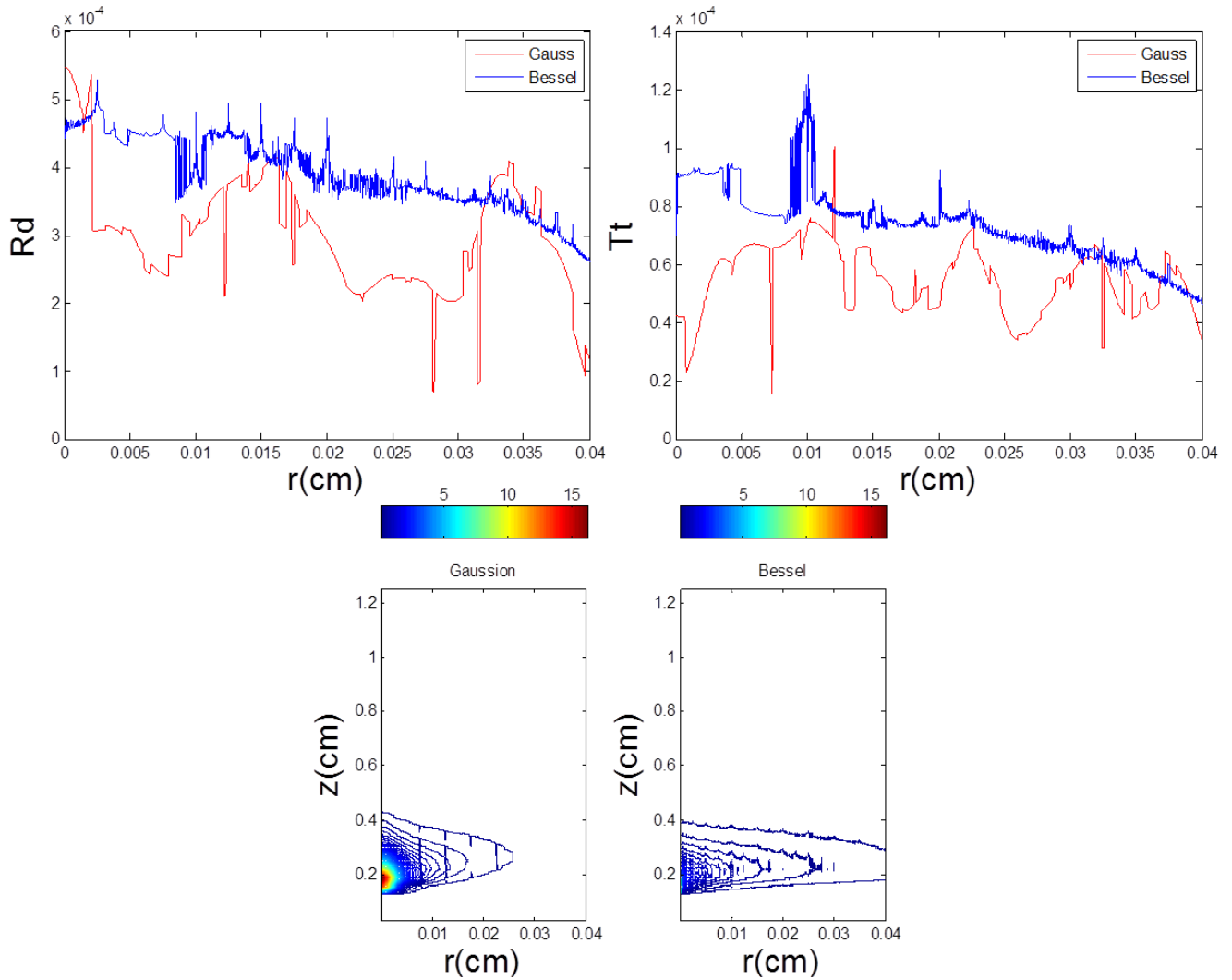


Figure 5.16 0.2% intralipid simulation results comparison: reflectance, transmittance and fluence

From the above figures, the results show that compared to Gaussian beams, Bessel beams have energy more concentrated at the incident point of the beam in terms of absorption. Besides, in each simulation, the average transmittance and reflectance from Bessel beam simulations are all greater than those from Gaussian beam simulations. Since the summation of transmittance, reflectance and absorption is the same, we can say the Bessel beam simulations have less absorption, which agrees with the observation from section 5.1.

## Chapter 6 Experimental investigation

This chapter describes the equipment and procedures of our experimental investigation of Bessel beam propagations in intralipid solutions with different concentrations. In section 6.1, we introduce the layout of the experimental setup and present calculations of the characteristics of the Bessel beam generated. Section 6.2 describes the experimental procedures.

### 6.1 Experimental setup

The experimental setup is shown in Figure 6.1. At the beginning, we use the laser as light source. After the laser, we use two lenses to make a telescope which expand the light by ten times ( $0.5 \text{ mm} \times 10$ ). The beam with a 5 mm diameter passes through the axicon. The generated Bessel beam penetrates the sample which is made of water and 10% intralipid solution combined in varying ratios and contained in a quartz cuvette. An imaging system which includes a microscope objective followed by a CMOS camera is used to measure the emerging beam from the cuvette. Tables 6.1 and 6.2 include the specifications of the components and the laser beam used respectively.

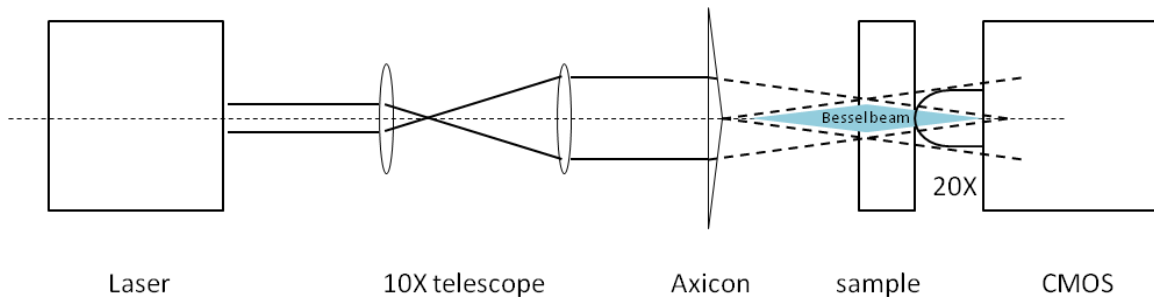


Figure 6.1 Experimental setup

### 6.1.1 Supplies

The supplies are listed in Table 6.1 and Table 6.2

Table 6.1 Supplies list

Component	Description
Axicon	Base angle $\alpha = 0.5^\circ$
Convex lens1	Focal length $f = 30$ mm
Convex lens2	Focal length $f = 300$ mm
Optical bench	
Various lens holders	
Quartz cuvettes	Wall thickness = 1.25 mm Inner size 10x10x40 mm
Intralipid10% solution	
Projector	Magnifying rate = 20
Digital camera	Resolution 640x480 Pixel size 11.2x11.2 $\mu\text{m}$

The laser specification is listed in a separate table below.

Table 6.2 Laser specification

Feature	Description
Laser type	diode-pumped solid- state (DPSS)
Wavelength	473 nm
Transverse Mode	TEM <sub>00</sub>
Output power	10.2 mW
$M^2$	1.1
Beam Size	0.53X0.44 mm
Beam divergence	1.4 mrad
Exit beam off angle	V
LD Operating Current	1480 mA
Power Stability	+/- 4.5%

### 6.1.2 Bessel beam specification

The depth of field (DOF) of the Bessel beam is approximated by

$$\text{DOF} \cong \frac{\omega_0}{2\beta} \quad (6.3)$$

where  $\omega_0$  is the laser beam diameter which is 5 mm and  $\beta$  is the refraction angle approximated by  $(n-1) \alpha = 0.0045$  radians. Therefore  $\text{DOF} = 0.5 (5 \text{ mm}) / 0.0045 = 555.56 \text{ mm} = 55.56 \text{ cm}$ . The other relevant characteristics of Bessel beams are the spot size and fringe spacing which are described in detail in Chapter 7.

## 6.2. Procedures and Methods

This section can be divided into two parts. In the first part, we are trying to make Bessel beams pass through intralipid samples with different concentrations and observe the beam profiles at exit from the sample by placing a CMOS camera against the sample cuvette's exit window. In the second part, we will move the sample cuvette along the depth of field (DOF) of the Bessel beams and see how the beam profile reconstructs.

### 6.2.1 Varying concentrations

Due to the limitation in terms of the maximum intensity which the CMOS would accept, we couldn't start the reference profile with a sample with only distilled water (intralipid 0%). So we experimented with the concentration to have it high enough to allow us to capture full distribution of the beam profile and low enough to get a clear image for analysis which means the light wouldn't be completely blocked by the sample due to scattering and absorption.

For example, an intralipid to water solution of 0.25% is considered too high of a concentration that the image doesn't show any clear light spot to analysis (Figure 6.2(a)). On the other hand, the maximum intensity value of the image from 0.05% intralipid solution experiment is too high and saturates the camera sensors. As a result, the plot of

the image will show a flat top as shown in Figure 6.2(b). Therefore, the range of the concentration we choose is from 0.1% to 0.2%.

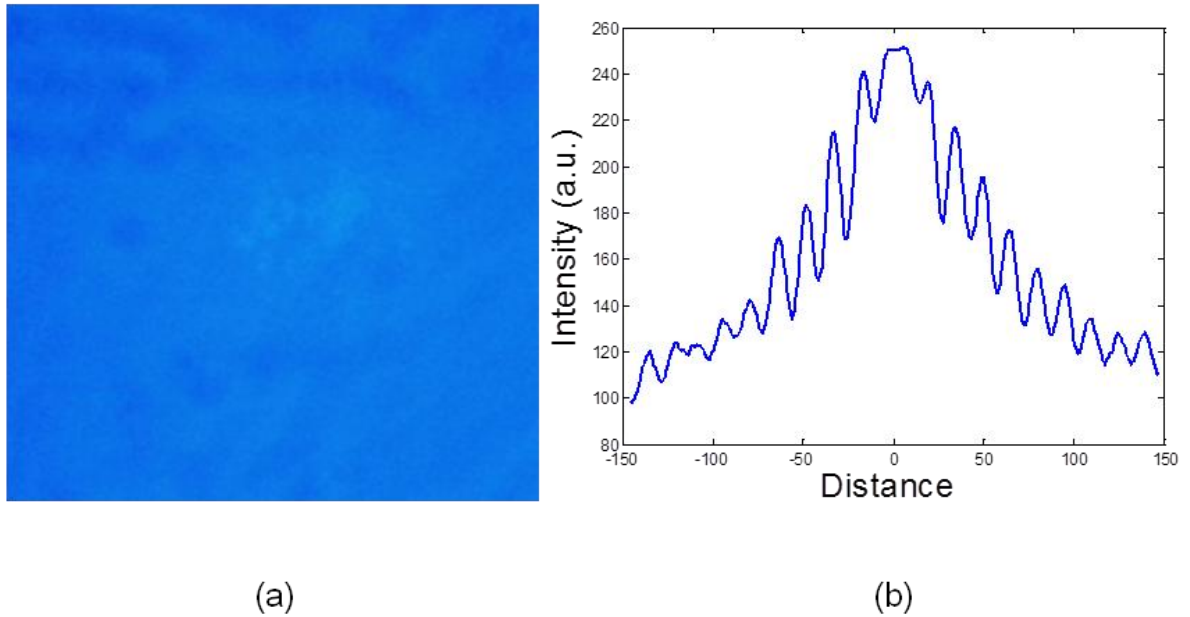


Figure 6.2 (a) Image from experiment with 0.25% intralipid. (b) Plot for image from with 0.05% intralipid

For the purpose of comparison, we choose 5 different concentrations within this range and the images are shown in Figure 6.3. From the image, we can see there are roughly seven fringes in the scanning area. From the calculation in chapter 7, the average fringe spacing is 0.005 cm. For the purpose of comparison with simulation results, we set the scanning radius to 0.04 cm.

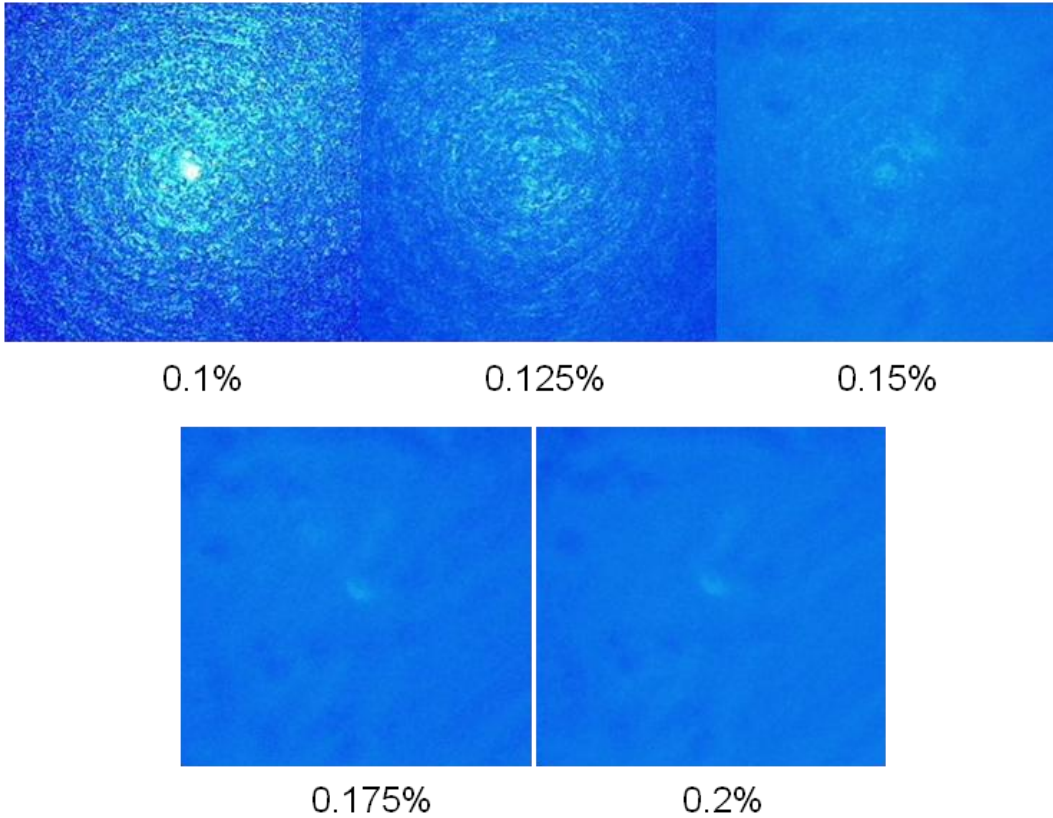
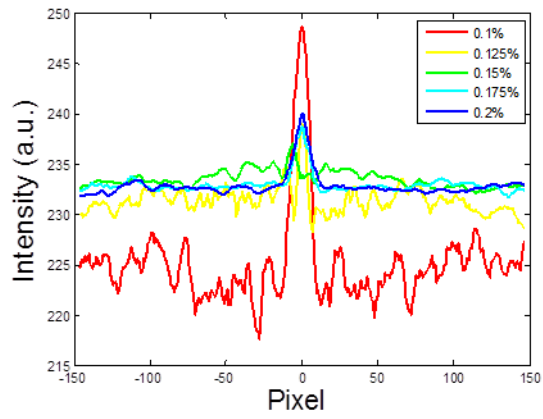
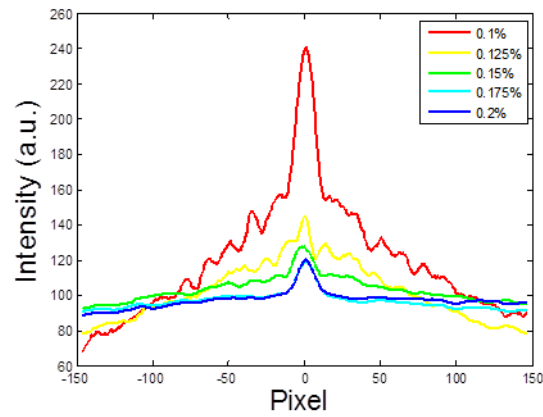


Figure 6.3 Images for different concentrations.

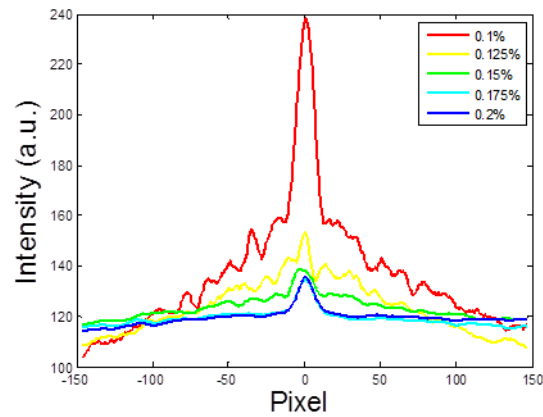
We use three different methods to “read” the image profile which is saved in the RGB format. Because we use a blue laser, which means the main color of the image would be blue, we firstly only take the blue color values into account. In the other two methods we calculate with full color profiles. The first one is to convert the image profile from color profile to gray profile before all the calculations. The second one is to keep the color image profile and then calculate the average values of red, blue, and green values on each pixel. The results are shown in Figure 6.4.



(a)



(b)



(c)

Figure 6.4 Comparison of blue laser Bessel beam profiles after propagation through 0.1% to 0.2% intralipid solutions. Profiles using: Image intensity using (a) Blue intensity, (b)

Gray intensity (c) Average red/blue/green (RBG) intensity

### 6.2.2 Self-healing property investigation

In principle, the self-healing property suggests that when the Bessel beam encounters an obstacle during its propagation through the sample, it should re-construct itself to the original profile after a short distance. Referring to Figure 6.5, by moving the cuvette, we would be able to change the distance,  $b$ , between the cuvette and the axicon as well as the distance,  $a$ , between the cuvette and the imaging system. Theoretically, the value of  $a$  is the distance along which beam re-constructs.

In this part, we move the sample to different positions along the axis of the Bessel beam within the range of the DOF (Figure 6.5). By definition, the intensity profile within the DOF of a Bessel beam doesn't change much. Therefore, as long as the sample is placed within the DOF, we assume the light at the exit of the sample should be the same. Taking advantage of this condition, we set the distance between the axicon and the image system to be 25 cm, which is within the DOF (55.56 cm). Because the path length of the cuvette is 1cm and we need to keep the cuvette at least 2 cm away from the axicon to allow the whole beam to enter the cuvette, the distance  $a$  is between 0 and 22 cm.

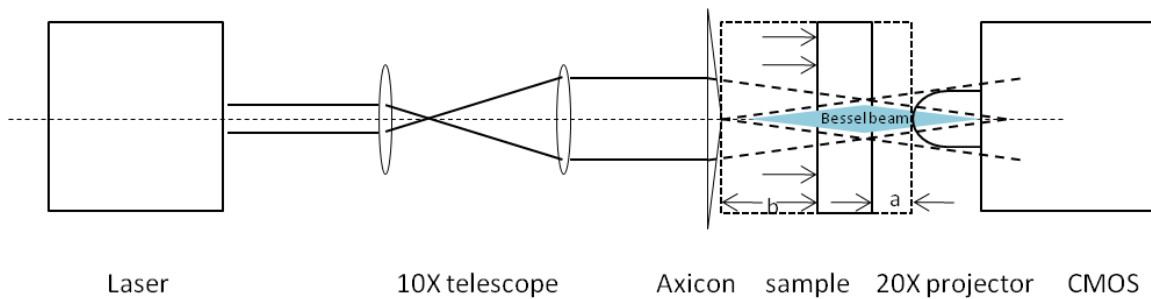


Figure 6.5 Experimental setup for self-healing property investigation

For the purpose of comparison, we choose 5 different positions within this range and the images and plots for 0.1% intralipid sample are shown in Figure 6.6 (the numbers in

the figure are the distance  $a$ ) and Figure 6.7 respectively. Following the same procedure, we repeat the experiment on samples with concentration at 0.125%, 0.15%, 0.175% and 0.2% (Figure 6.8-6.15).

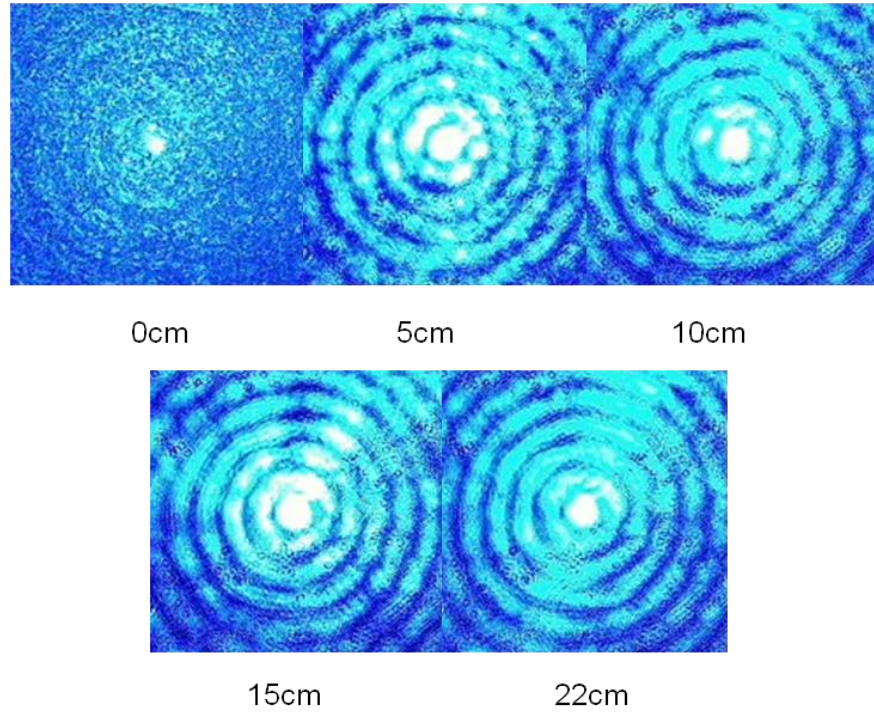


Figure 6.6 Images for 0.1% intralipid sample at different values of  $a$ .

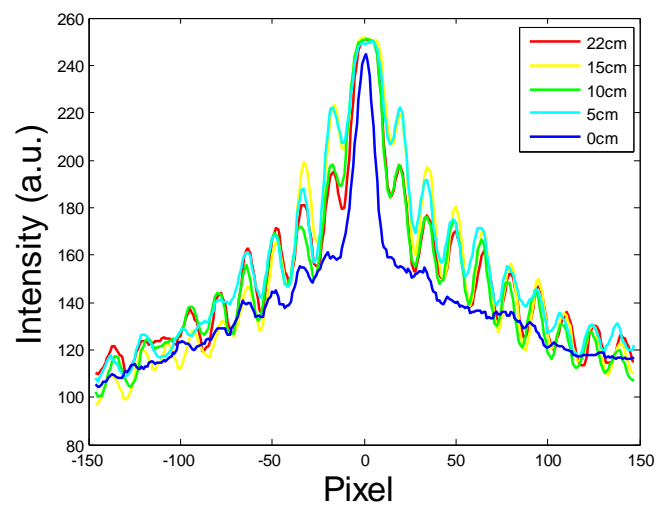


Figure 6.7 Comparison for 0.1% intralipid sample at different values of  $a$ .

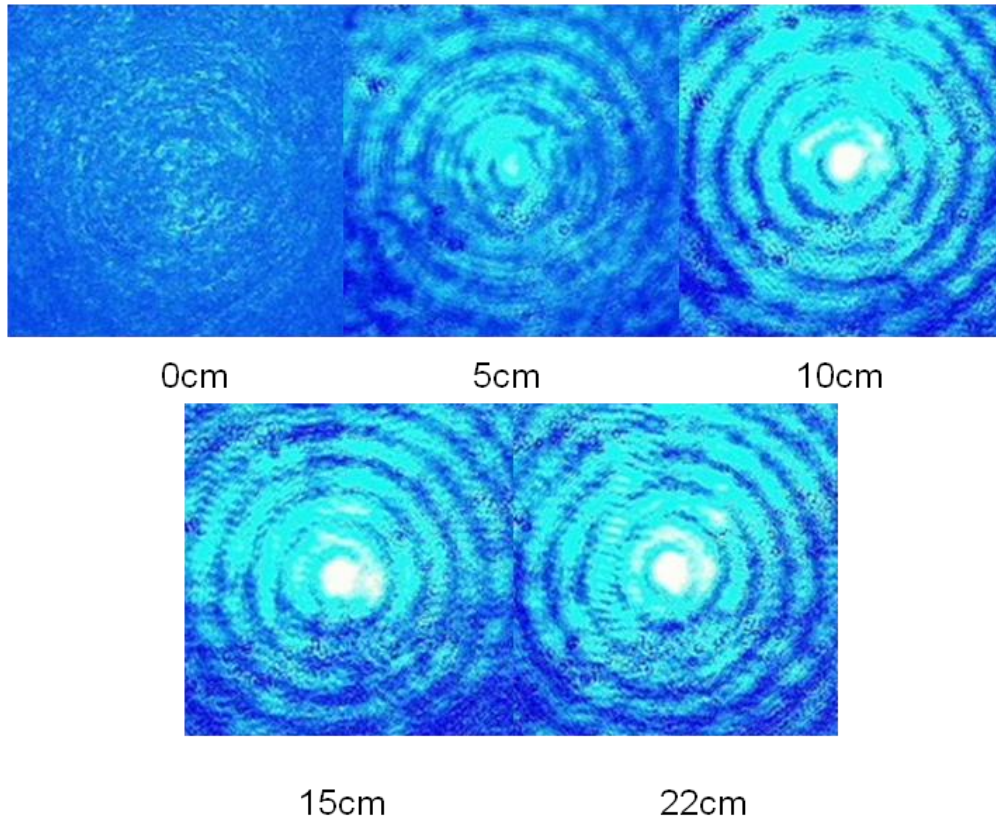


Figure 6.8 Images for 0.125% intralipid sample at different values of a.

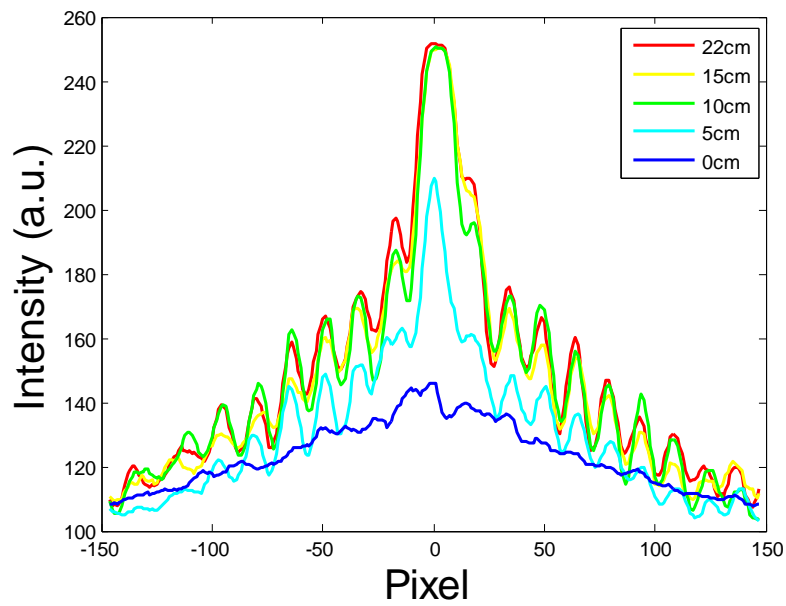


Figure 6.9 Comparison for 0.125% intralipid sample at different values of a.

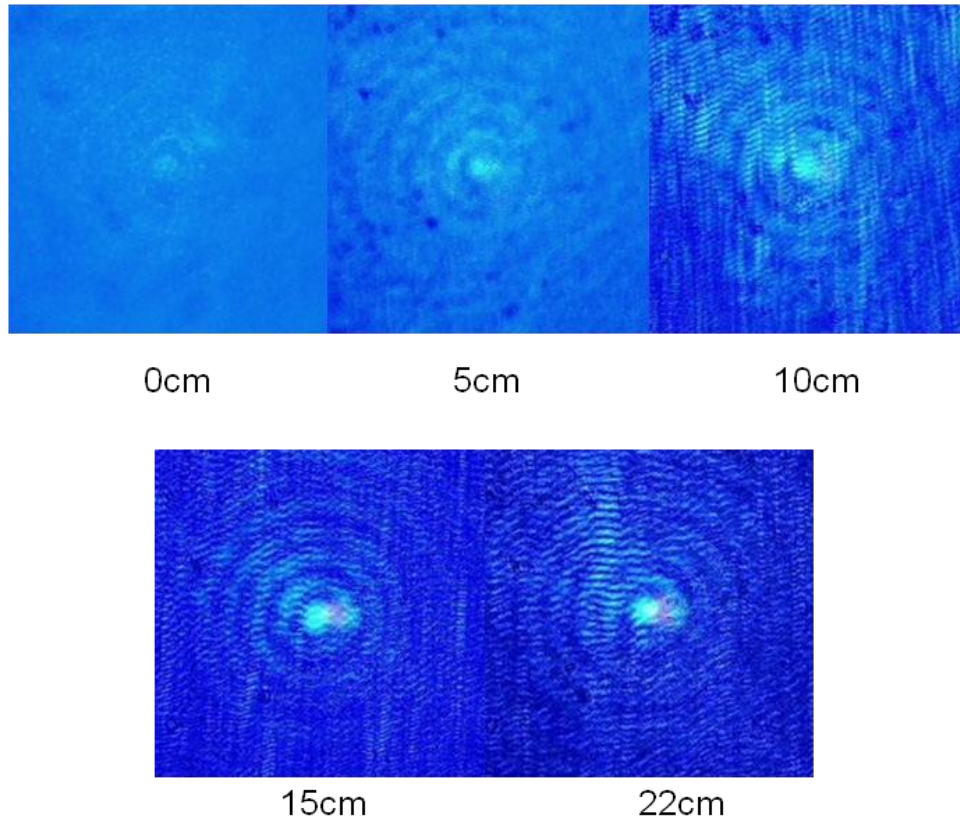


Figure 6.10 Image for 0.15% intralipid sample at different values of a.

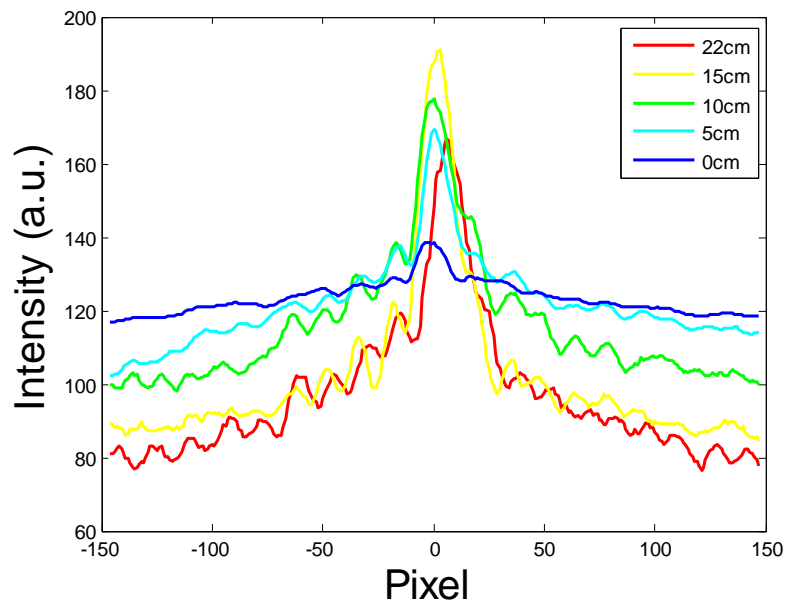


Figure 6.11 Comparison for 0.15% intralipid sample at different values of a.

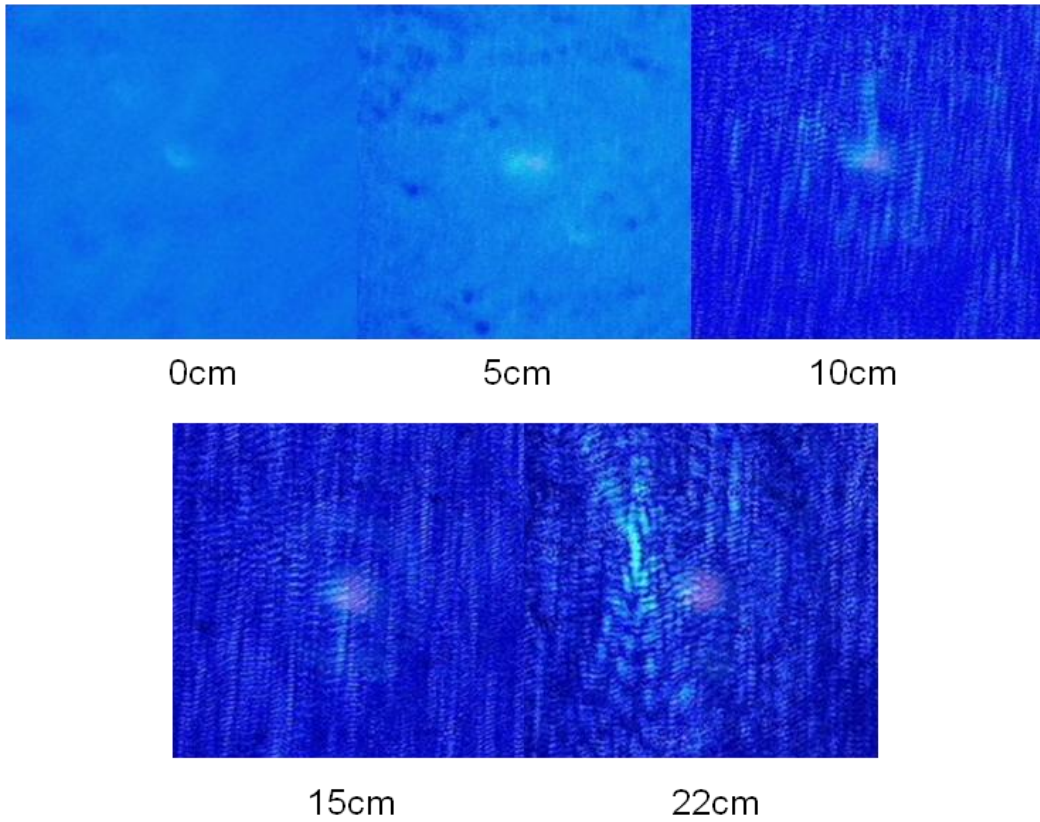


Figure 6.12 Image for 0.175% intralipid sample at different values of a.

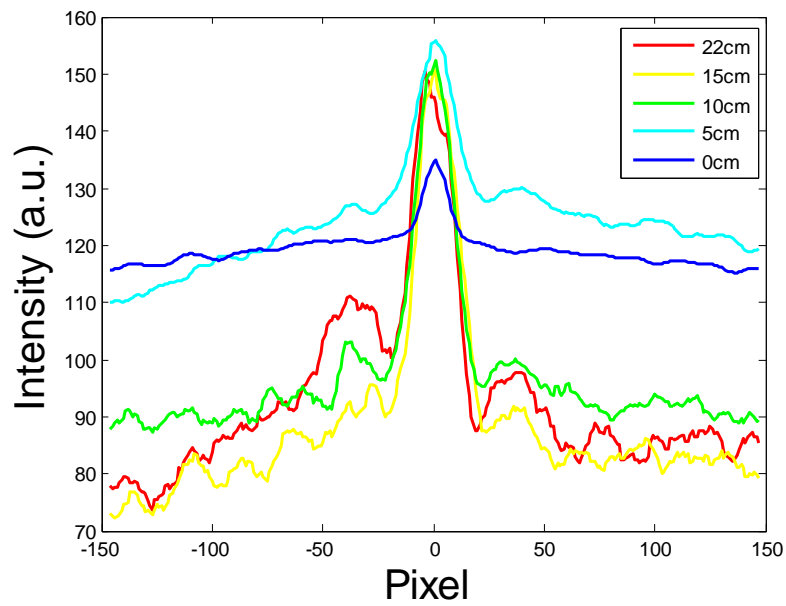


Figure 6.13 Comparison for 0.175% intralipid sample at different values of a.

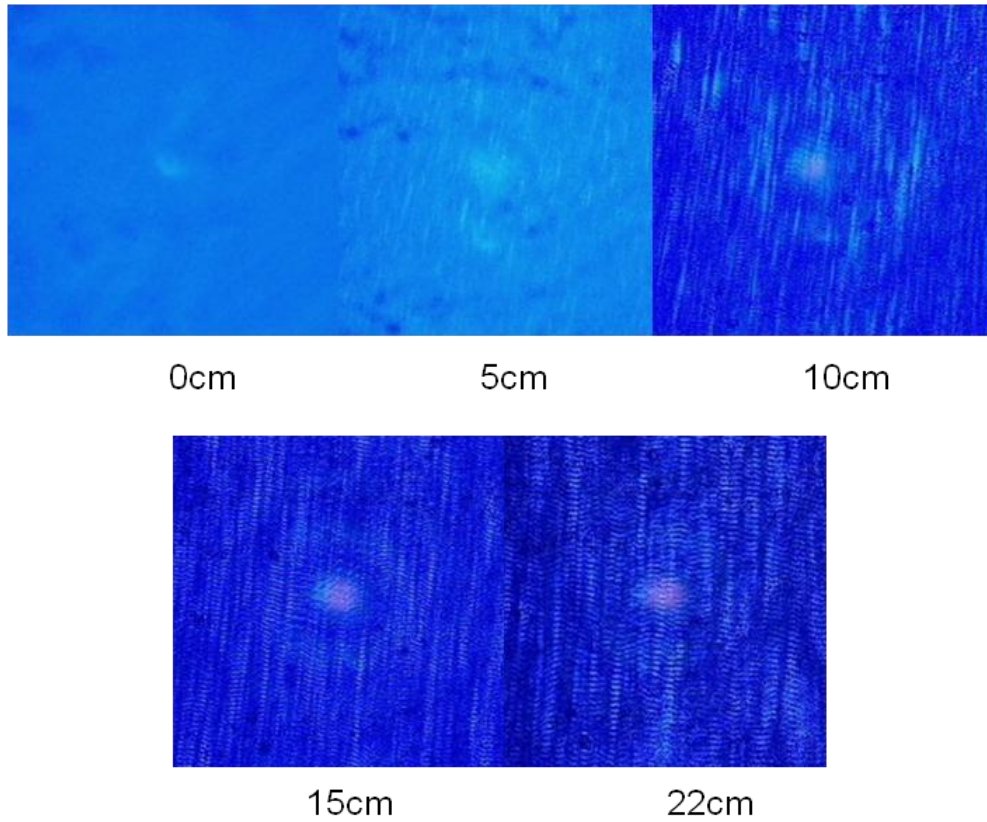


Figure 6.14 Image for 0.2% intralipid sample at different values of  $a$ .

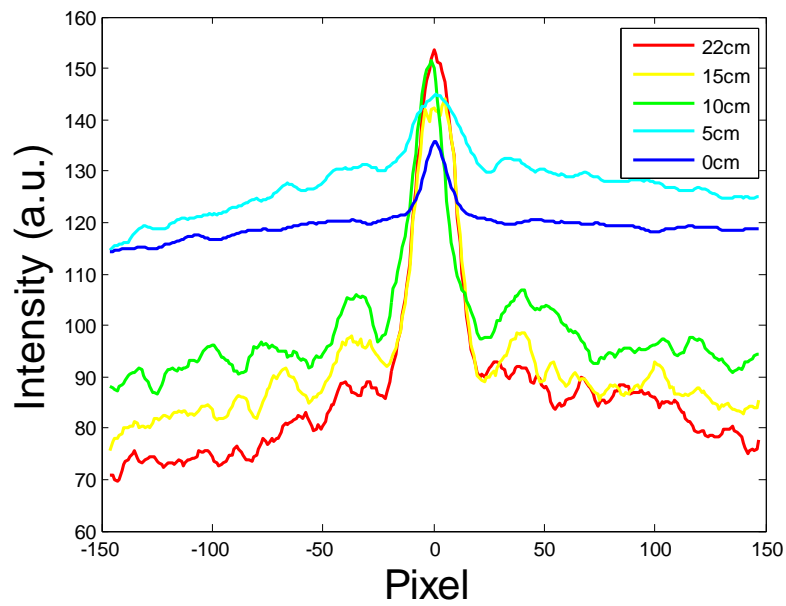


Figure 6.15 Comparison for 0.2% intralipid sample at different values of  $a$ .

## 6.4. Discussion

In the first part of the experiment (figures 6.3 & 6.4), the results show that both the total intensity and the maximum intensity drops as the concentration of the sample increases. After the concentration reached 0.175%, the image profile started to lose the feature of Bessel distribution. In the second part of the experiment (figures 6.6 to 6.15), the results mostly suggest the intensity is significantly weaker than the rest of the results when the cuvette is most close to the camera. However, there are two facts worth mentioning in this part of the experiment.

The first one is that the event of top flat plot occurred in the results for concentration 0.1% and 0.125% at positions close to axicon. The reason of this phenomenon is because the low concentrations, the CMOS sensor starts to saturate.

The other phenomenon we found from the results is that all the images for the experiments with position at 22 cm which is most close to the axicon don't have a well defined axis symmetrical shape. which is because, as we mentioned before, when the sample is too close to the axicon, not all the light converged from the axicon could come together to form the original Bessel profile or some of the photon practical entered the cuvette hit the side of it and reflect which is causing is irregular shape. This phenomenon can be found significantly in Figure 6.15.

## 6.5. Conclusion

Due to the limitations of the camera, we wouldn't get the full distribution of the image from distilled water as a reference line. However, the results quantitatively show how the intensity changes as the concentration (optical density) of the propagating media changes.

In the second part, the results show the beam intensity profile would stop changing and form the shape like the Bessel profile after a certain distance of propagation after the sample, which suggest the self-healing phenomenon.

## Chapter 7 Analysis

This chapter focuses on the analysis of the results obtained through both our experimental and numerical investigations. We divide this chapter into two parts. In the first part we discuss the experimental results obtained for the solutions with different intralipid concentrations. We quantitatively compare the experimental results to the simulation results in terms of total intensity. The second part focuses on the self-healing property of Bessel beams. We will quantitatively analyze the experimental results and estimate the required distance for self-reconstruction for the different concentrations.

### 7.1 Various concentrations

In this section, we first perform calculations for characterization of the Bessel beam and then we analyze the obtained experimental results. In calculation, we will theoretically define the spot size and the fringe spacing and compare them with the experimental results. And in the figure analysis, we integrate each curve to get total intensity for both simulation and experimental results and relate the total energy to the concentration of the intralipid solution.

#### 7.1.1 Bessel beam characterization

Beam radius

For a Bessel function distribution, the radius of the central lobe is given by [62]

$$r_0 = \frac{2.404\lambda}{2\pi\sin\beta} \quad (7.1)$$

where  $\lambda$  is the wavelength equal to 473 nm for the blue laser used and  $\beta$  is the refraction angle approximated by  $(n-1)\alpha$ . For a base angle  $\alpha = 0.5^\circ = 0.0087$  rad and index of

refraction  $n = 1.52$ , a value  $r_0 \approx 0.0039 \text{ cm}$  ( $40 \text{ }\mu\text{m}$ ) is obtained. To compare the propagation of Bessel and Gaussian beams we select comparable radii and similar energy based on the selected available axicon. The obtained Bessel beam radius is needed to determine a desirable Gaussian beam radius (chapter 5). To find the beam radius, typically, the FWHM (full width half maximum) or  $1/e^2$  definitions can be used.

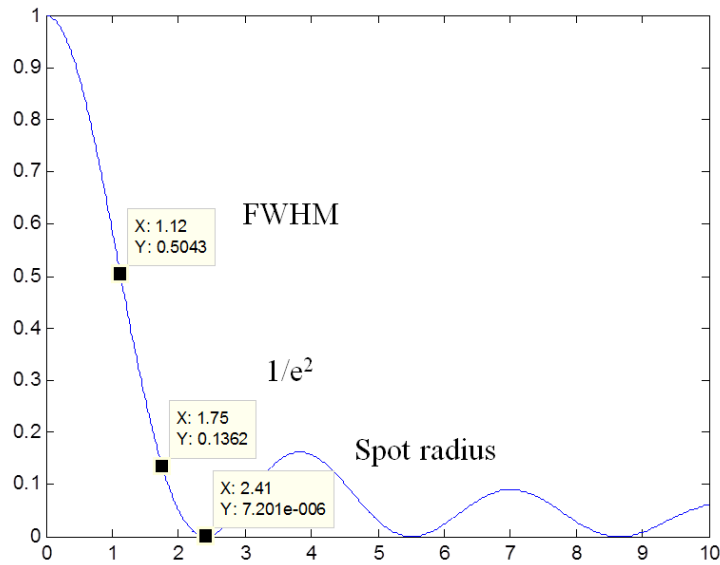


Figure 7.1 Bessel function plot showing the FWHM and  $1/e^2$  radii definitions.

As shown in Figure 7.1, the  $x$  coordinates for  $y = 0.5$  (FWHM),  $0.135(1/e^2$  width) and  $0$  ( $r_0$ ) are around 1.12, 1.75 and 2.41. In the present thesis, we use the  $1/e^2$  width method, giving

$$r = 0.73r_0 \quad (7.2)$$

Resulting in  $r = 0.73 \times 0.004 \text{ cm} = 0.029113 \text{ mm} \approx 0.003 \text{ cm}$

For a red laser ( $\lambda = 660 \text{ nm}$ ), apply the same method, the beam radius is determined to be  $0.0042 \text{ cm}$  (used in section 5.1&5.2).

## Spot size and fringe spacing

In order to determine the fringe spacing, we choose to plot the beam distribution and manually measure the  $x$  values of the points where intensity  $I = 0$ , which would include the points that define the spot size. In equation 4.6, the expression of the intensity of the Bessel beams, we set  $x = k\beta r$  and plot  $I = J_0^2(x)$  to find the root values shown in Figure 7.2. Using the roots we can calculate  $r$  given  $x = k\beta r$ , where  $k = 2\pi/\lambda$  then

$$r = \frac{x\lambda}{2\pi\beta} = \frac{473nm}{2\pi \cdot 0.0045} x = 0.0016 x \text{ cm} \quad (7.3)$$

The results are listed in Table 7.1. The spacing between the first two points is the spot size which is 0.0077 cm, which is similar to the result obtained from equation 7.1. In the last column of the table, we normalize the results by spot size to compare to the experimental values.

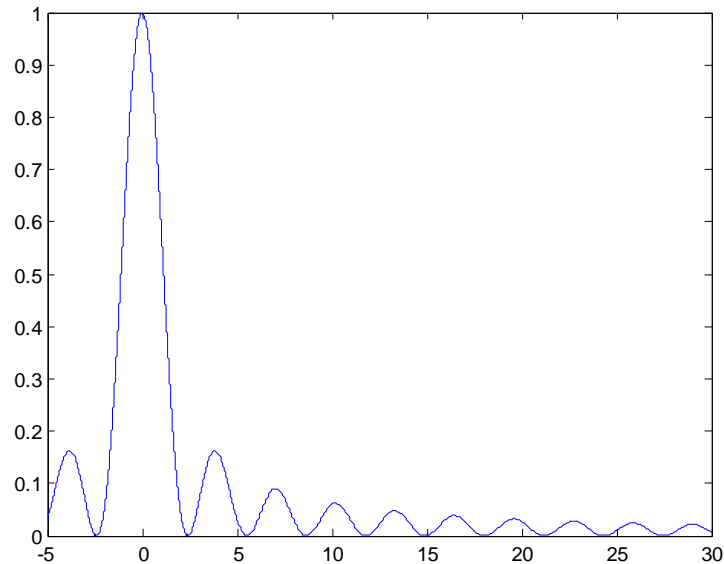


Figure 7.2 Bessel beam profile

Table 7.1 Theoretical fringe spacing for Bessel beams intensity

Point #	root	spacing	$r$ (cm)	Normalized $r$
1	-2.4	4.8	0.00768	1
2	2.4	3.11	0.004976	0.647917
3	5.51	3.15	0.00504	0.65625
4	8.66	3.18	0.005088	0.6625
5	11.84	3.11	0.004976	0.647917
6	14.95	3.16	0.005056	0.658333
7	18.11	3.19	0.005104	0.664583
8	21.3	3.06	0.004896	0.6375
9	24.36	3.16	0.005056	0.658333
10	27.52			

Then we manually measure the spot radius and fringe spacing on the figures we got from experiments. We select the two best developed profiles which are from the experiments with 0.1% and 0.15% concentrations of intralipid.

To measure these distances on the profile, we find all the valley points and find out their  $x$  axis coordinates. For the 0.1% intralipid figure, the results are shown in Figure 7.3.

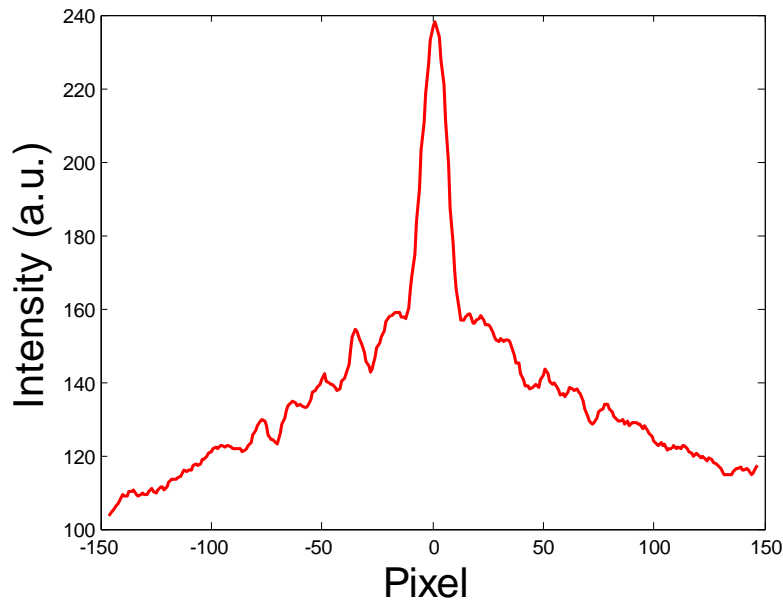


Figure 7.3 0.1% intralipid experiment result

We extract the  $x$  values from all the points into an array to analyze using excel as shown in Table 7.2. In order to compare the spacing, we normalize the results by the spot size to compare with the theoretical results as shown in Table 7.3.

Table 7.2 Spot radius and fringe spacing calculation from experimental profiles of Bessel beam exiting 0.1% intralipid solution.

point #	-6	-5	-4	-3	-2	-1	1	2	3	4	5	6	7
$x$ value	-84	-70	-57	-43	-28	-14	14	31	45	60	72	88	104
spacing	14	13	14	15	14	28	17	14	15	12	16	16	
Normalized spacing	0.5	0.46	0.5	0.53	0.5	1	0.61	0.5	0.53	0.43	0.57	0.57	0.5

The results are averaged from both sides of the central spot of the beam.

Table 7.3 Spacing results comparison

spacing	Spot size	Spacin g 1	Spacin g 2	Spacin g 3	Spacin g 4	Spacin g 5	Spacin g 6
Theoretical	1	0.65	0.66	0.66	0.65	0.66	0.66
Intralipid 0.1%	1	0.61	0.5	0.53	0.43	0.57	0.57

From Table 7.3, the fringe spaces of the experimental results can be considered consistent like the theoretical results. However, the average value of the spacing is smaller than the theoretical value. Since the data is normalized by the spot size, this could also mean the fringe spacing values are the same but the experimental spot size is larger than the theoretical spot size.

### 7.1.2 Comparison of simulation and experimental results

In this section, we attempt to compare the experimental and numerical simulation results for the interaction of the Bessel beam with intralipid solutions for different concentrations.

The experimental results we will be using are the profiles of Bessel beams exiting the cuvette containing the solutions, which are shown in Figure 7.5 (adapted from Figure 6.4). These results will be compared to the transmittance profiles obtained for the Bessel beams through simulation of propagation through the solutions with different concentrations. These profiles are shown in Figure 7.4. They represent measures of the simulated intensity profiles exiting the solutions. It can be clearly seen that the simulations do not reproduce the Bessel beam profiles obtained from the measurements. This is expected since the MCML and CONV software do not take into account diffraction as has been reported in the literature [41]. We can see however some similarities between the simulation and experimental results. Both the experimental and numerical intensity levels decrease with higher concentrations. In order to compare quantitatively these results, we integrate each profile over the whole area and we normalize with the maximum value. The results are shown in Figure 7.6. Also, we plot the maximum values of each profile as shown in Figure 7.7. From the calculations in chapter 3, we can see that the concentration and the optical density of the sample have a positive correlation, so that the results we obtain in this section also represent how the optical density of the medium affect the total transmittance of the propagation.

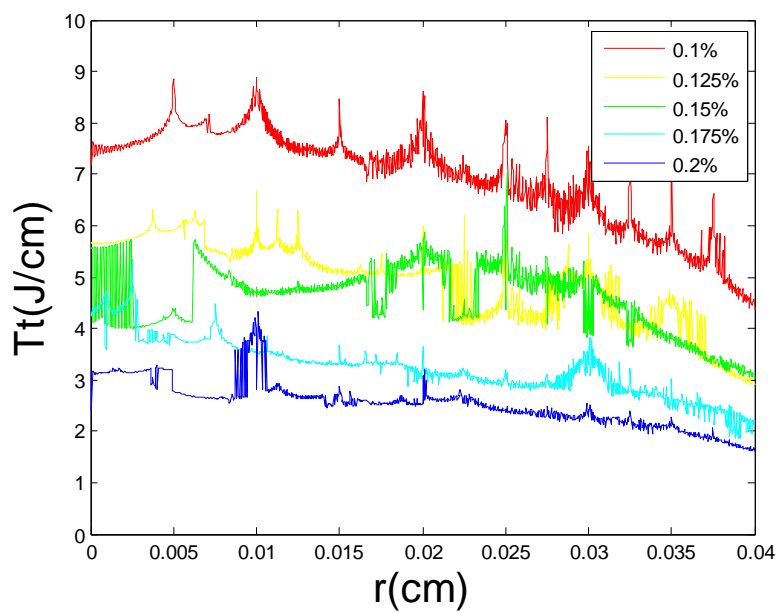


Figure 7.4 Simulation transmittance results for a Bessel beam of intralipid solutions

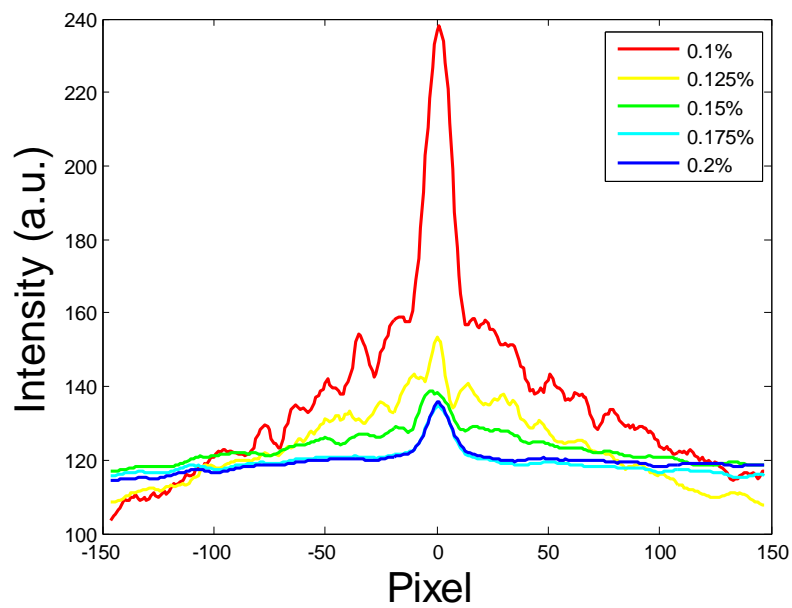


Figure 7.5 Experimental results for a Bessel beam of intralipid solutions

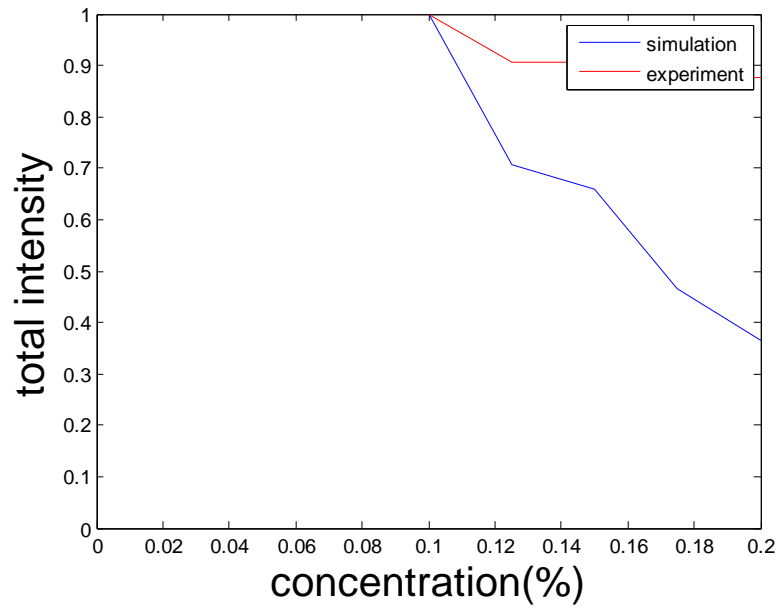


Figure 7.6 Total intensity from experiments and transmittance from simulation

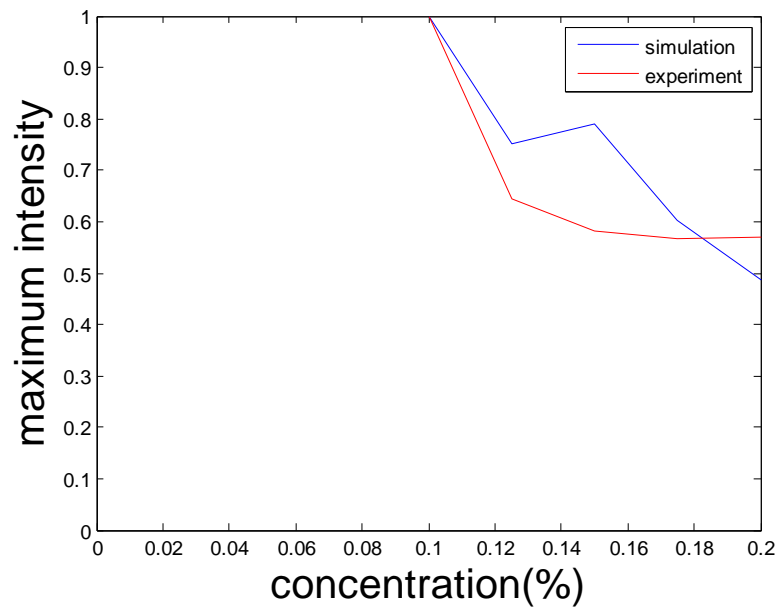


Figure 7.7 Maximum intensity from experiments and transmittance from simulation

## 7.2 Self-healing properties

### 7.2.1 Self-reconstructive region

According to Bouchal's experiments [4], the minimum self-healing distance of Bessel beam is the length of the shadow zone behind the obstacle and this length can be calculated by

$$L_{re} = Z_{shadow} = \frac{d}{2 \tan \beta} \approx \frac{d}{2 \beta} \quad (7.4)$$

Where  $Z_{shadow}$  is the shadow zone length and the  $L_{re}$  is the minimum distance for the beam to reconstruct. In our experiment, beam deviation angle is  $\beta = 0.0045$  rad and the obstacle size  $d$  is unknown. However, the two extreme bounding values for this parameter are defined as when we consider the obstacle as only one scattering particle in the solution or as the whole sample.

In the first case,  $d$  can be substituted as the average size of the satterer which is earlier mentioned to be 444 nm [25]. And therefore minimum distance for the beam to reconstruct after encountering this obstacle is calculated by equation 7.5.

$$L_{re1} = \frac{444 \text{ nm}}{2 \times 0.0045} = 0.049 \text{ mm}$$

In the other extreme case,  $d$  would be the outer dimension of the cuvatte which is 1.25 cm, giving

$$L_{re2} = \frac{1.25 \text{ cm}}{2 \times 0.0045} = 1.39 \text{ m}$$

The above values give bounding values for the minimum reconstructive distance of the Bessel beams.

### 7.2.2 Experimental results analysis

In chapter 6, we presented the experimental results in three different plotting methods which are blue, gray and RGB. Out of these three methods, the first one only considers the blue color signals from the image. Even though we use a blue laser, it doesn't mean the color of the laser exactly match the defined blue color from the software. As a result, this method will not be considered in further analysis. On the other hand, gray and RGB presentations are similar. Therefore, we only consider the figures generated by RGB method.

We determine the minimum distance for the beam to reconstruct  $L_{re}$  by evaluating the curves on each figure from the experiments on self-reconstruction. For example, from the results for 0.1% intralipid sample shown in Figure 7.8, we can see the curves red, yellow and green have very close shape but the cyan curve obviously is different from the three, so we can say the beam profile starts to reform to its original form at a point between position 0 cm to 5 cm. Therefore for 0.1% intralipid sample, the minimum distance for the beam to reconstruct  $L_{re}$  is 0~5 cm. The results in terms of positions are marked in the legend bar in each figure as shown below. Following the same procedures, the  $L_{re}$  values for all five different samples are shown in figures 7.8 to 7.12 and summarized in Table 7.4.

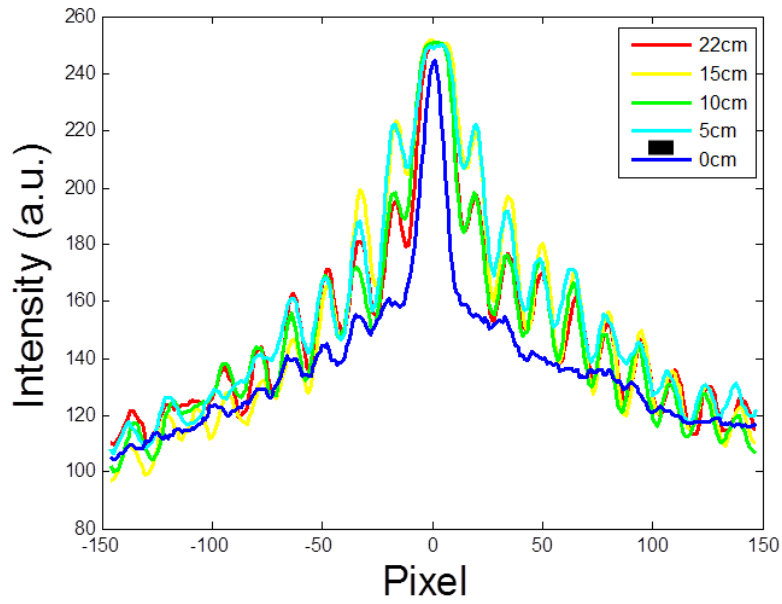


Figure 7.8 Comparison for 0.1% intralipid sample at different positions

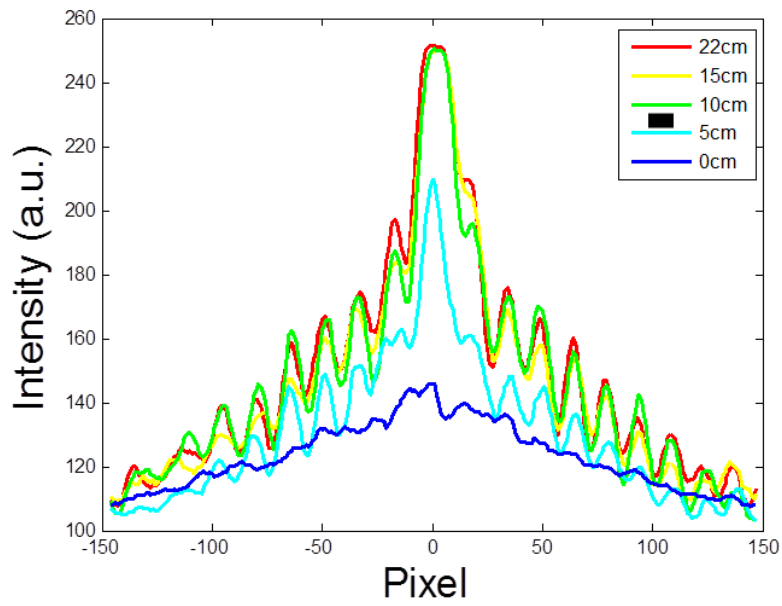


Figure 7.9 Comparison for 0.125% intralipid sample at different positions

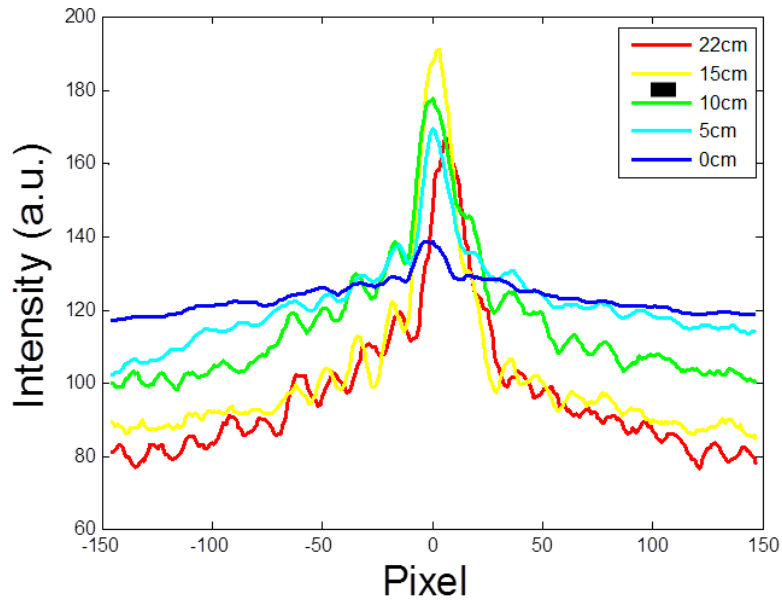


Figure 7.10 Comparison for 0.15% intralipid sample at different positions

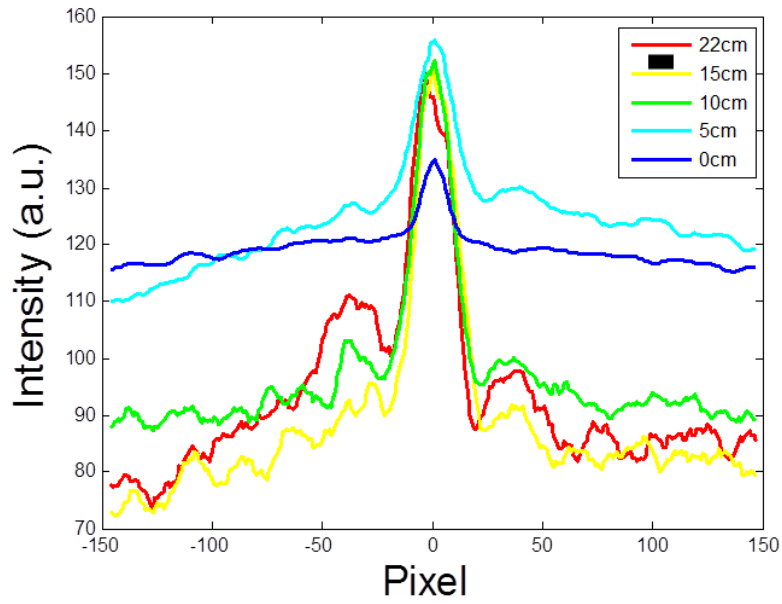


Figure 7.11 Comparison for 0.175% intralipid sample at different positions

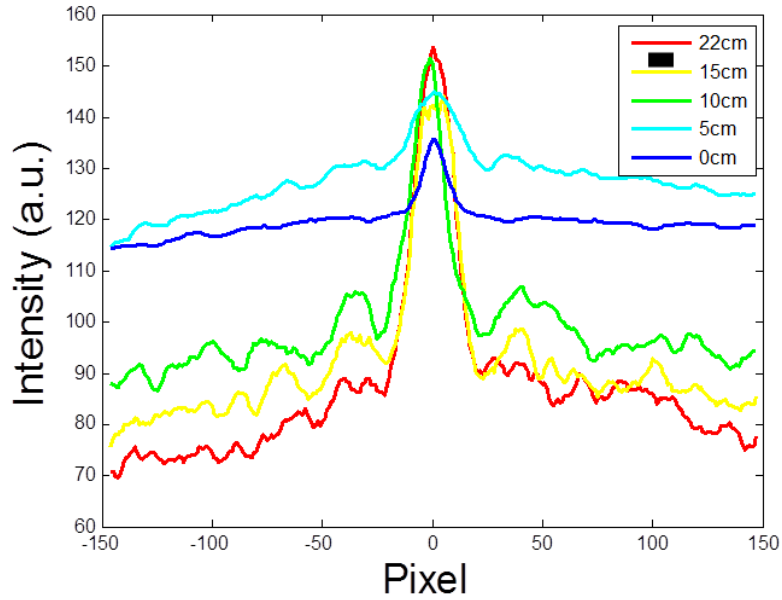


Figure 7.12 Comparison for 0.2% intralipid sample at different positions

Table 7.4 Minimum distance for the beam to reconstruct

Samples	Minimum $L_{re}$ (cm)	Maximum $L_{re}$ (cm)	Average $L_{re}$ (cm)
0.1% intralipid	0	5	2.5
0.125% intralipid	5	10	7.5
0.15% intralipid	10	15	12.5
0.175% intralipid	15	22	18.5
0.2% intralipid	15	22	18.5

From the result, we can see the figures 7.8, 7.11 and 7.12 have reached the boundaries of our testing range, which could mean the true results are out of boundaries. Besides, the results show that the minimum reconstructive distance increases as the concentration of the intralipid sample increases. So it suggests the minimum reconstructive distance is positively affected by the optical property of the propagating medium as shown in Figure 7.13.

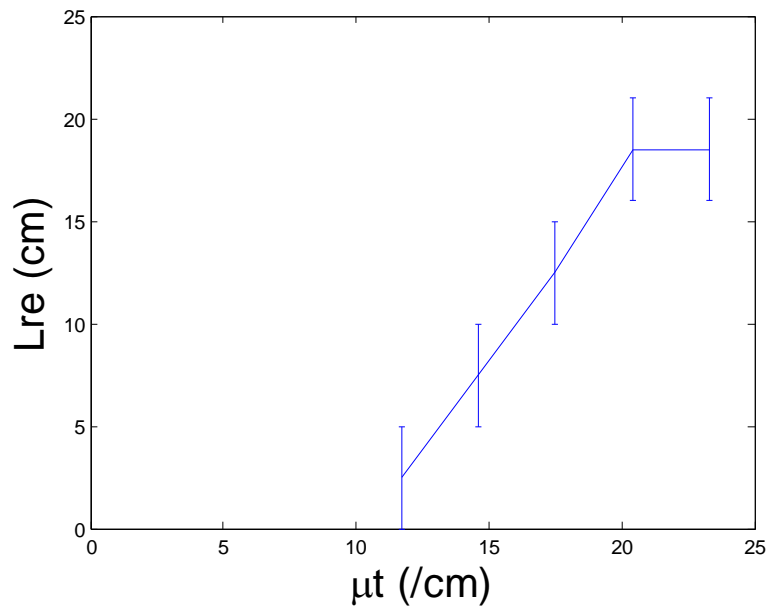


Figure 7.13 Minimum reconstructive distance related to optical property

## Chapter 8 Conclusions

In this work, we used Monte Carlo method based on the software MCML to study the propagations of Bessel and Gaussian beams. We modified the CONV program to be able to simulate the propagation of Bessel beams. We performed simulations as well as experiments for the propagation of Bessel beams within intralipid solutions.

The Monte Carlo method we used in this research convolves the responses of a propagation of a pencil beam with a beam intensity profile to simulate the propagation of a finite size beam. This process does not provide exact responses of the propagation because it doesn't model the diffraction behavior of light. However, the result could quantitatively represent the difference between the responses of different samples depend on their concentration.

The experimental results gave a quantitative measurement of the transmitted Bessel beam and its reconstruction after it exits the scattering media. The dependence of the reconstructive region on the optical property was measured.

In the future, since the main flaw of MCML is that it doesn't address the wave behaviour of light, we could modify the process based on the electric field theory [47] to increase the accuracy.

Regarding to the self-healing property investigation, the assumption was made that the intensity profile of the Bessel beam remain consistent within the DOF. This assumption is only true if the measurements were taken within a distance that is relatively smaller than the DOF, which is appropriate for the setup we presented in this thesis given the measurements were taken within 22 cm, which is considerably smaller than the DOF (55 cm). However, there were a couple of measurements suggest that we should extend the

measuring area. We cannot ignore the difference in the intensity profile caused by the positioning anymore if we do so. Therefore, a new setup of experiment is proposed. In this setup, we fix the cuvette at same location within the DOF so that the exit light of the cuvette will always be the same. The camera is moving along the optical line within the DOF to take measurements. While moving, the camera will take both images with cuvette present or not at each location. The images without the cuvette are used as reference data to compare to the images with the cuvette present to see how much the sample effect the overall result. The standard deviation is calculated as a factor to evaluate the difference between the images. The step size of the measurements is reduced to 1 cm from 5 cm. This setup would address the intensity profile difference caused by the positioning and provide more accurate results.

## Appendix A

### A.1 Optical properties determination for 10% intralipid solutions

We present an example of calculating the optical properties of 10% intralipid solutions for a wavelength of 473 nm using the fitting functions from [18]

#### A.1.1 Index of refraction

The formulation for index of refraction  $n$  is provided by the IAPWS (International Association for the Properties of Water and Steam). However, for room temperature and wavelengths over 400 nm, one can use Cauchy equation (3.6), to calculate the refractive index

$$n(\lambda) = I + \frac{J}{\lambda^2} + \frac{K}{\lambda^4} \quad (3.6)$$

where the numerical values of the coefficients are:  $J = 1.154 \times 10^4$ ,  $K = -1.132 \times 10^9$ ,  $I_{water} = 1.311$  and  $I_{soy} = 1.451$ . The wavelength is set to  $\lambda = 473$  nm. For the two main components of the solution

$$n_{water} = 1.311 + \frac{1.154 \times 10^4}{473^2} - \frac{1.132 \times 10^9}{473^4} = 1.34$$

$$n_{soy} = 1.451 + \frac{1.154 \times 10^4}{473^2} - \frac{1.132 \times 10^9}{473^4} = 1.48$$

It is assumed that the solutions are thoroughly mixed and that the mixture is of constant composition. Therefore, the refractive index is assumed to be proportionally related to the volumes of the compositions of the mixture, which can be written as

$$n = \frac{n_1 v_1 + n_2 v_2}{v_1 + v_2} \quad (3.7)$$

where  $v_1$ ,  $v_2$  and  $n_1$ ,  $n_2$  are the volumes and indices of refraction respectively of the two components. For 1 liter of 10% Intralipid, we have 100 g soybean oil, 22 g Glycerol and 12 g Eggphospholipid. Or  $m_{soy} = 100$  g,  $m_{Glycerol} = 22$  g and  $m_{egg} = 12$  g. Assume the refractive indices of other components are all identical to soybean oil. Then we can divide the mixture into two compositions which are Soybean oil, glycerol and eggphospholipid as the first composition and water as the second composition. The volume for first composition is calculated by

$$v_1 = \frac{m_{soy}}{\rho_{soy}} + \frac{m_{Glycerol}}{\rho_{Glycerol}} + \frac{m_{egg}}{\rho_{egg}} \quad (3.8)$$

where specific weight  $\rho_{soy} = 0.927$  g/ml and  $\rho_{Glycerol} = \rho_{egg} = 1$  g/ml

$$v_1 = \frac{100}{0.927} + \frac{22}{1} + \frac{12}{1} = 139.87 \text{ ml} \approx 0.14 \text{ L}$$

Since the total volume of the solution is one liter

$$v_2 = 1000 - v_1 = 860.13 \text{ ml (approximately)} \approx 0.86 \text{ L}$$

Substitute  $v_1$ ,  $v_2$ ,  $n_{water}$ ,  $n_{soy}$  in to equation 3.7

$$n \approx 1.48 \times 0.14 + 1.34 \times 0.86 = 1.36$$

### A.1.2 Absorption coefficient

The fitting function for  $\mu_a$  is

$$\mu_a = \frac{a}{1 + e^{-\frac{\lambda - x_0}{b}}} \quad (3.9)$$

The parameters are shown in Table 3.1.

Table 3.1 Parameters for calculation of the absorption coefficient

	$a$	$b$	$x_0$	$r^2$
water	$3.066 \times 10^5$	54.13	$1.770 \times 10^3$	0.9508
soy bean oil	$1.171 \times 10^5$	-36.59	$-3.210 \times 10^2$	0.9968

The total absorption coefficient is calculated by the sum of the single absorbers multiplied by their volume concentrations

$$\mu_{a(tot)} = \sum_{i=1}^n \mu_a(i) \sigma_a(i) \quad (3.10)$$

For water,  $\mu_a$  is given by

$$\mu_{a(water)} = \frac{3.066 \times 10^5}{1 + e^{-\frac{473 - 1.770 \times 10^3}{54.13}}} = 1.2037 \times 10^{-5} / mm = 1.2037 \times 10^{-4} / cm$$

For soy bean oil,  $\mu_a$  is given by

$$\mu_{a(soy)} = \frac{1.171 \times 10^5}{1 + e^{-\frac{473 + 3.21 \times 10^2}{-36.59}}} = 4.4096 \times 10^{-5} / mm = 4.4096 \times 10^{-4} / cm$$

The volume concentration of intralipid 10% is given by

$$C_v = \frac{c_w \rho_b}{c_w \rho_b + (1 - c_w) \rho_s} \quad (3.11)$$

Where  $\rho_w$  and  $\rho_s$  are specific weights of water and soybean oil which are 1g/cc and 0.92g/cc,  $C_w$  is the weight concentration of the sample which is 10%. So that  $C_v$  is determined to be 10.8%. The total coefficient of intralipid 10% is then given by

$$\mu_{a(tot)} = (1 - C_v) \mu_{a(water)} + C_v \mu_{a(soy)} \quad (3.12)$$

$$\mu_{a(tot)} = 1.55 \times 10^{-4} / cm$$

### A.1.3 Scattering anisotropy

The fitting function for  $g$  is

$$g(\lambda) = y_0 + a \cdot \lambda \quad (3.13)$$

The parameters are shown in Table 3.2.

Table 3.2 Parameters for calculation of the Scattering anisotropy

	Lipovenoes 10%	Lipovenoes 20%	ClinOleic 20%	Intralipid 10%	Intralipid 20%	Intralipid 30%
$y_0$	1.075	1.085	1.070	1.018	1.090	1.066
$a$	$-6.079 \times 10^{-4}$	$-6.029 \times 10^{-4}$	$-6.369 \times 10^{-4}$	$-8.820 \times 10^{-4}$	$-6.812 \times 10^{-4}$	$-4.408 \times 10^{-4}$
$r^2$	$9.997 \times 10^{-1}$	$9.992 \times 10^{-1}$	$9.999 \times 10^{-1}$	$9.926 \times 10^{-1}$	$9.995 \times 10^{-1}$	$9.982 \times 10^{-1}$

For Intralipid 10%:  $y_0 = 1.018$  and  $a = -8.820 \times 10^{-4}$ , giving:

$$g = 1.018 - 8.820 \times 10^{-4} \times 473 = 0.6008 \approx 0.6$$

#### A.1.4 Scattering coefficient

The fitting function for  $\mu_s$  is

$$\mu_s = a \cdot \lambda^b \quad (3.14)$$

The parameters are shown in Table 3.3.

Table 3.3 Parameters for calculation of the Scattering coefficient

	Lipovenoe s 10%	Lipovenoe s 20%	ClinOleic 20%	Intralipid 10%	Intralipid 20%	Intralipid 30%
$a$	$1.576 \times 10^8$	$3.116 \times 10^8$	$3.468 \times 10^8$	$4.857 \times 10^8$	$3.873 \times 10^8$	$2.645 \times 10^8$
$b$	-2.350	-2.337	-2.381	-2.644	-2.397	-2.199
$r^2$	$9.994 \times 10^{-1}$	$9.995 \times 10^{-1}$	$9.995 \times 10^{-1}$	$9.996 \times 10^{-1}$	$9.995 \times 10^{-1}$	$9.994 \times 10^{-1}$

For Intralipid 10%:  $a = 4.857 \times 10^8$  and  $b = -2.644$ , giving:

$$\mu_s = 4.857 \times 10^8 \times 473^{-2.644} = 41.1183 \approx 41/\text{mm} = 410/\text{cm}$$

In summary, the optical properties of 10% intralipid for a wavelength of 473nm are shown in Table 3.4.

Table 3.4 Optical properties of 10% intralipid under wavelength of 473nm

$n$	$\mu_a$	$g$	$\mu_s$
1.36	$4.3 \times 10^{-4}/\text{cm}$	0.6	410/cm

## Reference

- [1] Z. Song, K. Dong, X. Hu and J. Lu, "Monte Carlo simulation of converging laser beams propagating in biological materials," *Applied optics*, p. 2944, 1999.
- [2] A. Fowler and M. Menguc, "Propagation of focused and multibeam laser energy in biological tissue.," *Journal of Biomechanical Engineering*, p. 534, 2000.
- [3] D. McGloin and K. Dholakia, "Bessel beams: diffraction in a new light," *Contemporary Physics*, p. 15, 2005.
- [4] Z. Bouchal, J. Wagner and M. Chlup, "Self-reconstruction of a distorted nondiffracting beam," *Optics Communications*, p. 207, 2008.
- [5] M. Lin and Y. Yu, "A comparison of propagation between apertured Bessel and Gaussian beams," *Journal of Infrared, Millimeter, and Terahertz Waves*, p. 410, 2009.
- [6] K. Shinozaki, C. Xu, H. Sasaki and T. Kamijoh, "A comparison of optical second-harmonic generation efficiency using Bessel and Gaussian beams in bulk crystals," *Optics communications*, p. 300, 1997.
- [7] J. Broky, G. Siviloglou, A. Dogariu and D. Christodoulides, "Self-healing properties of optical Airy beams," *Optics express*, p. 12880, 2008.
- [8] T. Ersoy, B. Yalizay and S. Akturk, "Self-reconstruction of diffraction-free and accelerating laser beams in scattering media," *Journal of Quantitative Spectroscopy and Radiative Transfer*, p. 2470, 2012.

- [9] G. Siviloglou, J. Broky, A. Dogariu and D. Christodoulides, "Observation of accelerating Airy beams Observation of accelerating Airy beams," *Physical Review Letters*, p. 213901, 2007.
- [10] J. Durnin, J. Miceli and J. Eberly, "Comparison of Bessel and Gaussian beams," *Optics Letters*, p. 79, 1987.
- [11] G. Siviloglou, J. Broky, A. Dogariu and D. Christodoulides, "Ballistic dynamics of Airy beams," *Optics letters*, p. 207, 2008.
- [12] A. Saikaley, B. Chebbi and I. Golub, "Imaging properties of three refractive axicons," *Applied optics*, p. 6910, 2013.
- [13] B. Chebbi, S. Minko, N. Al-Akwaa and I. Golub, "Remote control of extended depth of field focusing," *Optics Communications*, p. 1678, 2010.
- [14] I. Golub, B. Chebbi, D. Shaw and D. Nowacki, "Characterization of a refractive logarithmic axicon," *Optics letters*, p. 2828, 2010.
- [15] L. Wang, S. Jacques and L. Zheng, "MCML—Monte Carlo modeling of light transport in multi-layered tissues," *Computer methods and programs in biomedicine*, 1995.
- [16] L. Wang, S. Jacques and L. Zheng, "CONV—convolution for responses to a finite diameter photon beam incident on multi-layered tissues," *Computer methods and programs in biomedicine*, p. 141, 1997.
- [17] S. Flock, S. Jacques, B. Wilson, W. Star and M. van Gemert, "Optical properties of Intralipid: a phantom medium for light propagation studies," *Lasers in surgery and*

*medicine*, p. 510, 1992.

- [18] R. Michels, F. Foschum and A. Kienle, "Optical properties of fat emulsions," *Optics Express*, p. 5907, 2008.
- [19] J. Cook, R. Bouchard and S. Emelianov, "Tissue-mimicking phantoms for photoacoustic and ultrasonic imaging.," *Biomedical optics express*, p. 3193, 2011.
- [20] L. V. Wang and H. Wu, *Biomedical Optics principles and Imaging*, Hoboken: John Wiley & Sons, 2007.
- [21] M. Lualdi, A. Colombo, B. Farina, S. Tomatis and R. Marchesini, "A phantom with tissue - like optical properties in the visible and near infrared for use in photomedicine," *Lasers in surgery and medicine*, p. 237, 2001.
- [22] G. Wagnières, S. Cheng, M. Zellweger, N. Utke, D. Braichotte, J. Ballini and H. van den Bergh, "An optical phantom with tissue-like properties in the visible for use in PDT and fluorescence spectroscopy," *Physics in medicine and biology*, p. 1415, 1997.
- [23] P. Di Ninni, F. Martelli and G. Zaccanti, "The use of India ink in tissue-simulating phantoms," *Optics express*, p. 26854, 2010.
- [24] J. Hebden, B. Price, A. Gibson and G. Royle, "A soft deformable tissue-equivalent phantom for diffuse optical tomography," *Physics in medicine and biology*, p. 5581, 2006.
- [25] I. Driver, J. Feather, P. King and J. Dawson, "The optical properties of aqueous suspensions of Intralipid, a fat emulsion," *Physics in medicine and biology*, p. 1927,

1989.

- [26] X. Wen, V. V. Tuchin, Q. Luo and D. Zhu, "Controlling the scattering of intralipid by using optical clearing agents," *Physics in medicine and biology*, p. 6917, 2009.
- [27] T. Ersoy, B. Yalizay, I. Cilesiz and S. Akturk, "Propagation of diffraction-free and accelerating laser beams in turbid media," *Atti della Accademia Peloritana dei Pericolanti-Classe di Scienze Fisiche, Matematiche e Naturali*, p. 89, 2011.
- [28] A. E. Karsten, A. Singh and M. W. Braun, "Experimental verification and validation of a computer model for light-tissue interaction," *Lasers in medical science*, p. 79, 2012.
- [29] K. Dong, Z. Song, J. Q. Lu and X. H. Hu, "Monte Carlo simulation of converging laser beams propagating in skin tissue phantoms," in *In BIOS'99 International Biomedical Optics Symposium*, 1999.
- [30] B. Wilson and G. Adam, "A Monte Carlo model for the absorption and flux distributions of light in tissue," *Medical physics*, p. 824, 1983.
- [31] S. A. Prahl, M. Keijzer, S. Jacques and A. J. Welch, "A Monte Carlo model of light propagation in tissue," *Dosimetry of laser radiation in medicine and biology*, p. 102, 1989.
- [32] H. Xu and M. S. Patterson, "Determination of the optical properties of tissue-simulating phantoms from interstitial frequency domain measurements of relative fluence and phase difference," *Optics express*, p. 6485, 2006.
- [33] V. Tsenova and E. Stoykova, "Refractive index measurement in human tissue

- samples," in *12th International School on Quantum Electronics Laser Physics and Applications*, 2003.
- [34] A. Ishimaru, *Wave propagation and scattering in random media*, New York: Academic press, 1978.
- [35] V. Tuchin, *Tissue optics: light scattering methods and instruments for medical diagnosis*, Bellingham: SPIE press, 2007.
- [36] J. H. McLeod, "Axicons and their uses," *JOSA*, p. 166, 1960.
- [37] G. Buffon, "Essai d'arithmetique morale," *Supplement a l'histoire naturelle*, p. 4, 1777.
- [38] M. J. C. Van Gemert, S. L. Jacques, H. J. C. M. Sterenborg and W. M. Star, "Skin optics," *IEEE Transactions on biomedical engineering*, p. 1146, 1989.
- [39] J. Schmitt, R. T. Wall, G. X. Zhou and E. C. Walker, "Multilayer model of photon diffusion in skin," *JOSA*, p. 2141, 1990.
- [40] I. D. Miller and A. R. Veitch, "Optical modelling of light distributions in skin tissue following laser irradiation," *Lasers in surgery and medicine*, p. 565, 1993.
- [41] B. H. Hokr, J. N. Bixler, G. Elpers, B. Zollars, R. J. Thomas, V. V. Yakovlev and M. O. Scully, "Modeling focusing Gaussian beams in a turbid medium with Monte Carlo simulations," *Optics express*, p. 8699, 2015.
- [42] C. M. Blanca and C. Saloma, "Monte Carlo analysis of two-photon fluorescence imaging through a scattering medium," *Applied optics*, p. 8092, 1998.
- [43] J. M. Schmitt and K. Ben-Letaief, "Efficient Monte Carlo simulation of confocal

- microscopy in biological tissue," *JOSA*, p. 952, 1996.
- [44] X. Gan and M. Gu, "Effective point-spread function for fast image modeling and processing in microscopic imaging through turbid media," *Optics letters*, p. 741, 1999.
- [45] X. Deng, X. Wang, H. Liu, Z. Zhuang and Z. Guo, "Simulation study of second-harmonic microscopic imaging signals through tissue-like turbid media," *Journal of biomedical optics*, p. 024013, 2006.
- [46] A. Leray, C. Odin, E. Huguet, F. Amblard and Y. Le Grand, "Spatially distributed two-photon excitation fluorescence in scattering media: Experiments and time-resolved Monte Carlo simulations," *Optics communications*, p. 269, 2007.
- [47] F. Cai and S. He, "Electric field Monte Carlo simulation of focused stimulated emission depletion beam, radially and azimuthally polarized beams for in vivo deep bioimaging," *Journal of biomedical optics*, p. 011022, 2014.
- [48] V. Kandidov, "Monte Carlo method in nonlinear statistical optics," *Physics-Uspeski*, p. 1243, 1996.
- [49] V. P. Kandidov, V. O. Militsin, A. V. Bykov and A. V. E. Priezhev, "Application of corpuscular and wave Monte-Carlo methods in optics of dispersive media," *Quantum Electronics*, p. 1003, 2006.
- [50] L. Margerin, M. Campillo and B. Tiggelen, "Radiative transfer and diffusion of waves in a layered medium: new insight into coda Q," *Geophysical journal international*, p. 596, 1998.

- [51] A. Klose, U. Netz, J. Beuthan and A. H. Hielscher, "Optical tomography using the time-independent equation of radiative transfer—Part 1: forward model," *Journal of Quantitative Spectroscopy and Radiative Transfer*, p. 691, 2002.
- [52] R. C. Haskell, L. O. Svaasand, T. T. Tsay, T. C. Feng, B. J. Tromberg and M. S. McAdams, "Boundary conditions for the diffusion equation in radiative transfer," *JOSA A*, p. 2727, 1994.
- [53] Y. Cai, Y. Chen, H. Eyyubođlu and Y. Baykal, "Propagation of laser array beams in a turbulent atmosphere," *Applied Physics B*, p. 467, 2007.
- [54] Y. Chen and J. Liu, "Characterizing the beam steering and distortion of Gaussian and Bessel beams focused in tissues with microscopic heterogeneities," *Biomedical optics express*, p. 1318, 2015.
- [55] Oregon Medical Laser Center, "Home," 2016. [Online]. Available: <http://omlc.org/software/>. [Accessed 26 10 2016].
- [56] wolfram, "convolution," [Online]. Available: <http://mathworld.wolfram.com/Convolution.html>. [Accessed 20 10 2016].
- [57] WolframAlpha, [Online]. Available: [https://www.wolframalpha.com/input/?i=integral+x\\*besselj\(0,x\)%5E2](https://www.wolframalpha.com/input/?i=integral+x*besselj(0,x)%5E2). [Accessed 25 10 2016].
- [58] WolframAlpha, [Online]. Available: [https://www.wolframalpha.com/input/?i=besselj\(m,x\)](https://www.wolframalpha.com/input/?i=besselj(m,x)). [Accessed 25 10 2016].
- [59] I. Malitson, "Interspecimen Comparison of the Refractive Index of Fused Silica\*t,"

*Journal of the optical society of America*, p. 1205, 1965.

[60] R. Olson, "Human carotid artery wall thickness, diameter, and blood flow by a noninvasive technique," *Journal of applied physiology*, p. 955, 1974.

[61] School of Anatomy and Human Biology - The University of Western Australia, "Integumentary System," 26 10 2016. [Online]. Available:

<http://www.lab.anhb.uwa.edu.au/mb140/CorePages/Integumentary/Integum.htm>.

[62] Doric lenses, "Axicon," [Online]. Available:

<http://www.doriclenses.com/lire/46.html>. [Accessed 29 8 2012].

[63] C. K. Hayakawa, E. O. Potma and V. Venugopalan, "Electric field Monte Carlo simulations of focal field distributions produced by tightly focused laser beams in tissues," *Biomedical optics express*, p. 278, 2011.